

# Angle-resolved photoemission spectroscopy and its application to topological materials

Baiqing Lv<sup>1,2</sup>, Tian Qian<sup>1,3,4\*</sup>  and Hong Ding<sup>1,3,4\*</sup>

**Abstract** | Angle-resolved photoemission spectroscopy (ARPES) — an experimental technique based on the photoelectric effect — is arguably the most powerful method for probing the electronic structure of solids. The past decade has witnessed notable progress in ARPES, including the rapid development of soft-X-ray ARPES, time-resolved ARPES, spin-resolved ARPES and spatially resolved ARPES, as well as considerable improvements in energy and momentum resolution. Consequently, ARPES has emerged as an indispensable experimental probe in the study of topological materials, which have characteristic non-trivial bulk and surface electronic structures that can be directly detected by ARPES. Over the past few years, ARPES has had a crucial role in several landmark discoveries in topological materials, including the identification of topological insulators and topological Dirac and Weyl semimetals. In this Technical Review, we assess the latest developments in different ARPES techniques and illustrate the capabilities of these techniques with applications in the study of topological materials.

Understanding the collective behaviour of electrons in solids is increasingly desirable as these electronic interactions give rise to many intriguing phenomena in condensed matter physics, such as superconductivity<sup>1,2</sup> and quantum Hall effects<sup>3–7</sup>. The nature of electrons in solids is described primarily by three quantum parameters: energy ( $E$ ), momentum ( $k$ ) and spin ( $S$ ). Owing to its unique capability to probe the energy and momentum of electrons directly and simultaneously, angle-resolved photoemission spectroscopy (ARPES)<sup>8–10</sup> has a leading role in achieving a comprehensive understanding of the electronic properties of solid-state materials.

With the rapid development of electron spectrometers<sup>11</sup>, modern synchrotrons<sup>12–18</sup> and laser light sources<sup>19–25</sup> over the past three decades, ARPES has experienced a renaissance. The notable improvement in energy and momentum resolution<sup>21,22</sup> with laser light sources not only enables fine features of electronic states, such as the energy gap in superconductors, to be measured with unprecedented precision<sup>26</sup>, but also makes it possible to obtain information on many-body interactions in strongly correlated systems<sup>27–29</sup>. The use of continuously tunable soft X-rays greatly enhances the bulk sensitivity of ARPES<sup>12,16,30–32</sup>; high sensitivity is crucial for studying the bulk electronic structure of 3D materials, especially that of topological semimetals<sup>33–37</sup>. The integration of spin detectors into ARPES photoelectron spectrometers has further extended the capability of

ARPES<sup>38–42</sup>, enabling quantification of the spin polarization of band structures<sup>43–47</sup>. Moreover, the emergence of light sources with microscale or even nanoscale spot sizes has given rise to the possibility of performing spatially resolved ARPES measurements<sup>48–51</sup>, which will have a central role in probing the electronic structure of microscale and nanoscale materials as well as materials with phase separation or multiple domains<sup>52–54</sup>. Finally, the implementation of time-resolved ARPES with ultrafast lasers or X-ray sources<sup>20,55–59</sup> makes it possible to study ultrafast electronic dynamics in the time domain<sup>60–68</sup> and enables the unoccupied states above the Fermi level ( $E_F$ )<sup>69–71</sup> to be probed. The advances in ARPES have made it an effective and ideal tool for the identification of the unique bulk and surface electronic structures of topological materials. Topological materials thus serve as excellent examples to illustrate the capability of different ARPES techniques.

Three-dimensional topological materials are usually characterized by the nature of the surface states induced by the topology of the bulk band structure, which can be divided into two groups with respect to the bulk bandgap: insulators with non-zero bandgaps (for example, topological insulators<sup>43,44,72–77</sup> and topological crystalline insulators<sup>78–82</sup>) and semimetals with no bandgaps (for example, Dirac semimetals<sup>83–87</sup> and Weyl semimetals<sup>33,34,37,88–95</sup>). Taking advantage of different ARPES techniques, such as vacuum ultraviolet (VUV, with

<sup>1</sup>Beijing National Laboratory for Condensed Matter Physics and Institute of Physics, Chinese Academy of Sciences, Beijing, China.

<sup>2</sup>Department of Physics, Massachusetts Institute of Technology, Cambridge MA, USA.

<sup>3</sup>CAS Centre for Excellence in Topological Quantum Computation, University of Chinese Academy of Sciences, Beijing, China.

<sup>4</sup>Songshan Lake Materials Laboratory, Dongguan, China.

\*e-mail: tqian@iphy.ac.cn; dingh@iphy.ac.cn

<https://doi.org/10.1038/s42254-019-0088-5>

## Key points

- Topological materials are characterized by non-trivial bulk and surface electronic states, which can be detected and distinguished by angle-resolved photoemission spectroscopy (ARPES).
- Synchrotron-based vacuum ultraviolet and soft-X-ray light make it possible to distinguish surface and bulk states through photon-energy-dependent ARPES measurements.
- The integration of spin detectors into ARPES photoelectron spectrometers enables the detection and quantification of spin polarization in band structures.
- Time-resolved ARPES with femtosecond laser pulses facilitates the study of ultrafast electronic dynamics and states above the chemical potential.
- Spatially resolved ARPES with sub-micrometre spatial resolution can be used to probe the electronic structure of microscale and nanoscale materials as well as materials with phase separation or multiple domains.

a photon energy in the range 6–124 eV), soft-X-ray (with a photon energy between 124 eV and 5 keV) and spin-resolved ARPES, researchers have made several landmark discoveries in topological materials in recent years. In this Technical Review, we focus principally on the latest developments in different ARPES techniques. To illustrate the capabilities of these techniques, we highlight recent results from several topological materials, including the well-known  $\text{Bi}_2\text{Se}_3$  family of topological insulators<sup>44,74,75</sup> and the TaAs family of Weyl semimetals<sup>33,34,37,90,91,95</sup>.

## Fundamentals of ARPES

The basics of ARPES have been described in detail elsewhere<sup>8–10,96–100</sup>. In the following section, we provide a brief introduction to salient points that are useful in understanding ARPES studies of topological materials.

ARPES is based on the photoelectric effect, which was first discovered by Hertz in 1887 (REF.<sup>101</sup>); the microscopic mechanism of this effect was later explained by Einstein in 1905 (REF.<sup>102</sup>), when he introduced the concept of a quantum of light — the photon. In a typical ARPES measurement, a sample is placed under ultra-high vacuum next to an electron analyser (FIG. 1a). When light is incident on the sample, electrons in the material absorb photons, and if the energy of the absorbed photons is greater than the work function of the material, the electrons can escape into the vacuum. These photoemitted electrons, known as photoelectrons, are then collected and analysed with respect to their kinetic energy and emission angle by a spectrometer. The energy and momentum of the electrons inside the sample are directly connected to those of the photoelectrons by the conservation of energy and momentum parallel to the sample surface. Under the emission angles  $\theta$  and  $\varphi$  defined in FIG. 1a, the following relationships hold (Eq. 1 and 2).

$$E_{\text{kin}} = h\nu - \Phi - E_{\text{B}} \quad (1)$$

Here,  $E_{\text{kin}}$  is the kinetic energy of a photoelectron;  $h\nu$  is the photon energy;  $E_{\text{B}}$  is the binding energy of the electron inside the sample; and  $\Phi$  is the work function of the material, which is the energy required for an electron at  $E_{\text{F}}$  to escape to the vacuum level ( $E_{\text{vac}}$ ) (where  $\Phi = E_{\text{vac}} - E_{\text{F}}$ ; FIG. 1b).

$$\begin{aligned} \hbar k_{\parallel}^{\text{f}} &= \hbar k_{\parallel}^{\text{i}} \\ &= \sqrt{2mE_{\text{kin}}} \left( \sin\theta \cos\varphi \hat{k}_x + \sin\theta \sin\varphi \hat{k}_y \right) \end{aligned} \quad (2)$$

where  $\hbar k_{\parallel}^{\text{f}}$  and  $\hbar k_{\parallel}^{\text{i}}$  are the parallel components (with respect to the sample surface) of the momenta of the photoelectron and the initial electron, respectively;  $\theta$  and  $\varphi$  are the emission angles of the photoelectron;  $\hbar$  is the reduced Planck's constant; and  $m$  is the electron rest mass. The above conservation laws are valid provided that the relaxation time of the electron–hole pairs is much longer than the escape time of the photoelectrons (of the order of several tens of attoseconds)<sup>103</sup> and the momentum of the photons ( $\sim 0.015 \text{ \AA}^{-1}$  at a typical photon energy of 30 eV) is much smaller than the momentum of the photoelectrons<sup>8</sup>.

The momentum perpendicular to the surface,  $k_{\perp}$ , is not conserved because the surface of the material necessarily breaks the translational symmetry in this direction (thus,  $k_{\perp}^{\text{f}} \neq k_{\perp}^{\text{i}}$ , where  $k_{\perp}^{\text{f}}$  and  $k_{\perp}^{\text{i}}$  are the perpendicular components of the momenta of the photoelectron and initial electron, respectively). However,  $k_{\perp}^{\text{i}}$  can still be extracted by using a nearly free-electron approximation for the final states, which is a reasonable approximation for a sufficiently high photon energy (usually tens to hundreds of eV)<sup>8,104–106</sup>:

$$k_{\perp}^{\text{i}} = \sqrt{2m(E_{\text{kin}} \cos^2\theta + V_0)} / \hbar \quad (3)$$

where  $V_0$  is a constant called the inner potential.  $V_0$  can be determined from photon-energy-dependent measurements by fitting the experimental periodicity along the  $k_{\perp}$  direction<sup>30,104–106</sup>. Once  $V_0$  has been determined, the value of  $k_{\perp}^{\text{i}}$  can be extracted. Therefore, photon-energy-dependent ARPES measurements are an effective way to probe the electronic structure in the 3D Brillouin zone; this capability is crucial for studying topological materials.

Strictly, the photoemission process corresponds to a quantum many-body propagator that describes the single-particle removal function from the full Fermi sea and can be fully described by the so-called one-step model<sup>8,9</sup>. However, the one-step model is complicated, as it treats photoemission as a single coherent process and thus describes the bulk, surface and evanescent states within a single Hamiltonian. In many simplified cases, ARPES data are discussed within the context of the three-step model<sup>8,9</sup>, which separates photoemission into three sequential processes: photon absorption, electron transport to the surface, and emission of the electron into the vacuum. In addition, the so-called sudden approximation is typically assumed, which means that the electron is assumed to be instantaneously removed from the solid and to have no further interaction with the system left behind.

Under the framework of the three-step model and the sudden approximation, the ARPES photoemission intensity  $I(\mathbf{k}, E)$  can be written as

$$I(\mathbf{k}, E) = I_0(\mathbf{k}, \nu, A) A(\mathbf{k}, E) f(E, T) \quad (4)$$

where  $A(\mathbf{k}, E)$  is the one-particle spectral function from which it is possible to extract information about the

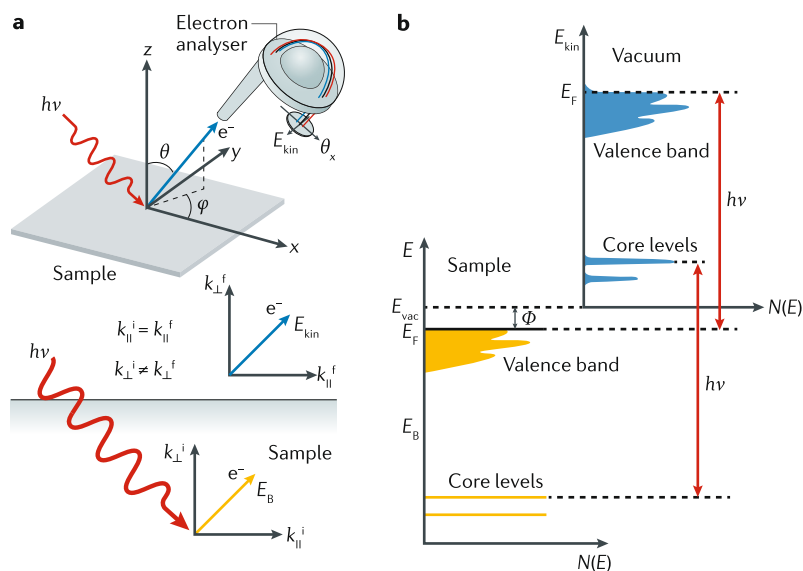


**Fig. 1 | Fundamentals of ARPES measurements.** **a** | Illustration showing the geometry and basic principles of angle-resolved photoemission spectroscopy (ARPES) measurements. Under incidence of light with photon energy  $h\nu$ , electrons are ejected from the surface of a sample at an angle  $(\theta, \varphi)$  and collected with an electron analyser (top part). The bottom part shows the momentum conservation of electrons. In the photoemission process, translational symmetry in the direction parallel to the sample surface is preserved. Thus, the in-plane momentum ( $k_{\parallel}$ ) is conserved; that is,  $k_{\parallel}^i = k_{\parallel}^f$  (where  $i$  and  $f$  indicate the initial and final states, respectively). By contrast, the momentum in the direction perpendicular to the surface ( $k_{\perp}$ ) is not conserved, such that  $k_{\perp}^i \neq k_{\perp}^f$ . **b** | Energetics of the photoemission process, in which energy is conserved:  $E_{\text{kin}} = h\nu - \Phi - E_{\text{B}}$ , where  $h\nu$  is the photon energy,  $\Phi$  is the work function,  $E_{\text{B}}$  is the binding energy of the electron inside the sample and  $E_{\text{kin}}$  is the kinetic energy of the photoelectron.  $E$ , energy;  $E_{\text{F}}$ , Fermi level;  $E_{\text{vac}}$ , vacuum level;  $N(E)$ , density of states. Panel **a** is adapted with permission from REF.<sup>8</sup>, APS.

quasiparticle self-energy that encodes the band structure and correlation effects, and  $f(E, T)$  is the Fermi–Dirac distribution (where  $T$  is the temperature). The first term on the right-hand side  $I_0(\mathbf{k}, \nu, \mathbf{A}) \propto \sum_{f,i} |M_{f,i}^k|^2$ , where  $M_{f,i}^k = \phi_f^k | \mathbf{A} \cdot \mathbf{P} | \phi_i^k$  is the photoemission matrix element, which describes the transition of the initial state  $\phi_i^k$  to the final state  $\phi_f^k$ .  $\mathbf{P}$  is the electronic momentum operator, and  $\mathbf{A}$  is the electromagnetic vector potential, which depends on the photon polarization and energy. The matrix element carries no direct information on the band dispersion. However, the matrix element can provide important orbital information on electronic states if specific measurement geometries are implemented (see Supplementary Information for further information) and has been used widely in the study of, for example, iron-based superconductors<sup>107–109</sup>.

### VUV ARPES

An important parameter of ARPES is the incident photon energy. In the past few years, the energy range of photons has greatly expanded, owing to the development of laser and synchrotron light sources. At present, the incident light used varies from VUV light to soft and even hard X-rays. Among these, the most commonly used is VUV light.

The universal curve of the inelastic mean free path of a photoelectron as a function of its kinetic energy<sup>110</sup> (FIG. 2a) shows that for incident photon energies above 20 eV in the VUV region, the mean free path is short ( $<0.6$  nm).

Thus, ARPES is an extremely surface-sensitive technique, and a considerable fraction of the total ARPES signal will be representative of only the topmost surface layer of a sample. This surface sensitivity is an advantage when the aim is to probe surface states, such as those in topological insulators and Weyl semimetals, but requires ARPES experiments to be performed on atomically clean and well-ordered flat surfaces. To obtain a clean surface and to avoid surface contamination, single crystals are typically cleaved in situ and measured in ultrahigh vacuum chambers, but even then, the freshly cleaved surface has a finite measurement lifetime. To maximize the sample measurement time, it is necessary to use a vacuum with pressures lower than  $5 \times 10^{-11}$  Torr, which can be routinely achieved by using modern ultrahigh-vacuum systems. Although flat mirror-like surfaces can be obtained through straightforward cleaving for many materials, there are numerous materials that are not cleavable (especially 3D materials), which limits the applicability of ARPES. As an alternative to cleaving, freshly prepared thin films can be used, and it has now become routine to grow films in vacuum and transfer them immediately to an ARPES chamber after growth. Indeed, many ARPES systems have been developed that incorporate thin-film growth capabilities, such as those for molecular beam epitaxy and pulsed laser deposition; numerous achievements, such as the characterization of the electronic structure in high-critical-temperature (high- $T_c$ ) superconducting FeSe films<sup>29,111–113</sup> and the metallic surface and interface states in oxide insulators<sup>47</sup>, have been enabled by these combined systems. Another powerful way to prepare atomically clean and flat surfaces is the polish–sputter–anneal method, in which samples are polished, repeatedly sputtered and then annealed<sup>114</sup>. This method is suitable for certain materials that have strong chemical bonding, the surfaces of which can crystallize via annealing in vacuum. Recently, the polish–sputter–anneal method was applied to the study of the CoSi family of 3D topological semimetals<sup>115,116</sup> and enabled the observation of multiple types of unconventional chiral fermions and helical Fermi arc surface states on the (001) surface.

For VUV ARPES, there are three types of light sources that have been successfully used: noble-gas discharge lamps<sup>117</sup>, synchrotron radiation<sup>12–18</sup> and lasers<sup>19–25</sup>. At present, these three VUV light sources are complementary for ARPES experiments; their main features are summarized in TABLE 1 and are discussed in the following sections.

### Lamp-based VUV ARPES

As the earliest photoemission light sources, noble-gas discharge lamps have been used widely in laboratory-based ARPES systems. These lamps use gas resonance lines as monochromatic light sources. A common example is the modern helium lamp, in which the radiation is generated through the microwave plasma technique<sup>118</sup>. Such a helium lamp mainly provides two discrete photon energies, 21.2 eV (He Ia) and 40.8 eV (He IIa), which can be selected by adjusting the angle of a diffraction grating in a monochromator. Additionally, the monochromator refocuses the beam to a spot size of  $\sim 1$  mm with a typical flux of  $\sim 10^{12}$  photons per second.

#### Fermi arc

An open contour at the Fermi energy, arising from a chiral surface state owing to the non-trivial topology of band-crossing points in bulk states.

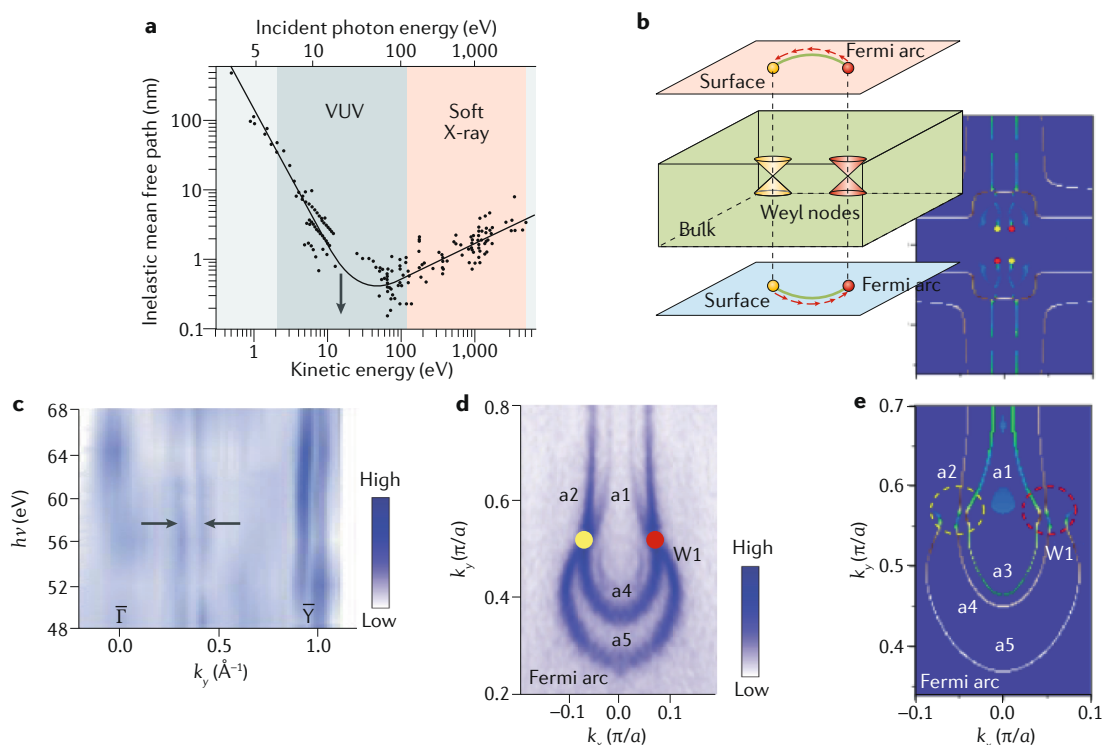


**Fig. 2 | Synchrotron-based VUV ARPES in the study of TaAs surface states.** Synchrotron-based vacuum ultraviolet (VUV) angle-resolved photoemission spectroscopy (ARPES) is a surface-sensitive technique that has been used to probe the surface states of Weyl semimetals, leading to the identification of Fermi arcs on the (001) surface of TaAs. **a** | Plot showing the universal curve of the inelastic mean free path of photoelectrons as a function of kinetic energy (bottom axis) and incident photon energy (top axis; calculated on the assumption that materials have a typical work function of 4 eV and electrons are located at the Fermi level). Coloured regions correspond to the typical photon energy ranges of VUV and soft-X-ray light. **b** | Schematic of a Weyl semimetal with spin-polarized Fermi arcs on its surfaces. The Fermi arcs connect the projections of two Weyl nodes of opposite chirality (indicated by the red and yellow points). The red arrows on the surfaces indicate the spin texture of the Fermi arcs. **c** | ARPES intensity plot of TaAs at the Fermi level ( $E_F$ ) along the  $\bar{\Gamma}$ – $\bar{\Gamma}$  direction as a function of photon energy ( $h\nu$ ). The observed Fermi surfaces (which appear as vertical lines, such as those indicated by the arrows) are constant despite variations in the photon energy, indicating that they are surface states. **d** | ARPES intensity plot at  $E_F$  recorded on the (001) surface of TaAs ( $k_y$  and  $k_x$  are the momenta in the  $y$  and  $x$  directions, respectively). The yellow and red dots indicate the projection of Weyl points  $W1$  of opposite chirality. In panels **d** and **e**, a1–a5 are five different Fermi surfaces. **e** | Calculations of the surface states of TaAs at  $E_F$  around Weyl points  $W1$  of opposite chirality (indicated by dashed circles as the chemical potential is slightly away from the nodes) along the  $\bar{\Gamma}$ – $\bar{\Gamma}$  direction. Panel **a** is adapted with permission from REF.<sup>110</sup>, Wiley-VCH. Panel **b** is adapted with permission from REF.<sup>45</sup>, APS. Panels **c** and **d** are adapted from REF.<sup>37</sup>, Springer Nature Limited. Panel **e** is adapted from REF.<sup>91</sup>, CC-BY-3.0.

In comparison to the other two VUV sources, discharge lamps are compact, and the beam position and intensity are stable. More importantly, the photon energy provided by discharge lamps is suitable for typical ARPES experiments, owing to reasonable photoemission cross sections<sup>8,9,119</sup> (~2 Mb per atom for Au with He I $\alpha$  light) and a negligible space-charge effect<sup>120–122</sup>. However, discharge lamps have several limitations: relatively low photon flux (especially for high-resolution measurements) compared with a 7 eV laser<sup>21,22</sup>, non-tunable photon energy with fixed or no polarization, a requirement of very flat sample surfaces owing to the large beam spot size, and leakage of noble gas into the ARPES chamber during measurements. Nevertheless, noble-gas discharge lamps are still the most popular and favourable laboratory-based light sources, and are particularly useful in the study of layered materials and thin films<sup>111–113</sup>, which usually have large flat surfaces that can accommodate the large photon beam spot.

### Synchrotron-based VUV ARPES

When electrons travelling at relativistic velocities are bent by a static magnetic field, strong electromagnetic radiation is emitted owing to the radial component of acceleration. This synchrotron radiation light can be applied to ARPES once correctly monochromatized. Indeed, benefiting from the continued development of synchrotron technology, especially the advent of third-generation synchrotron light sources, many synchrotron-based ARPES end-stations have been built and have gradually become the most powerful ARPES systems over the past 30 years<sup>12–18</sup>.

Synchrotron-based ARPES has many notable advantages. First, by using a variable polarization undulator and high-resolution monochromator, the photon energy and high-resolution monochromator, the photon energy and polarization (linear or circular) of the beam can be readily tuned. The continuously tunable photon energy makes it possible to map the electronic structure in the entire 3D momentum space and to distinguish the

#### Space-charge effect

The spectral redistribution of the energy and momentum of photoelectrons induced by Coulombic repulsion.

Table 1 | Comparison of the three types of ARPES light sources

Light source	Photon energy	Best energy resolution (meV)	Photon flux (photons per second)	Beam spot size	Polarization	Detection range
Laser	Discrete values or discretely tunable within a limited range of several eV to tens of eV	<1 (REFS <sup>21,22</sup> )	$\sim 10^9$ – $10^{15}$	$\sim 100$ $\mu\text{m}$	Tunable	First to second Brillouin zones
Synchrotron	Continuously tunable from several eV to thousands of eV	1–30 (REFS <sup>13,16</sup> )	$\sim 10^{12}$ – $10^{13}$	Tens of nanometres <sup>49</sup> to hundreds of micrometres	Tunable	Several Brillouin zones
Discharge lamp	Discrete values between several eV and tens of eV <sup>a</sup>	$\sim 1$ <sup>b</sup>	$\sim 10^{12}$	$\sim 1$ mm	Non-tunable	First to second Brillouin zones

ARPES, angle-resolved photoemission spectroscopy. <sup>a</sup>Examples of common discharge lamps include the He lamp (with photon energies of 21.2 eV for He I $\alpha$  and 40.8 eV for He II $\alpha$ ) and the Xe lamp (with a photon energy of 8.4 eV for Xe I). <sup>b</sup>Data for the VUV5k He lamp.

surface and bulk states by performing photon-energy-dependent ARPES measurements<sup>33,34,75,91</sup>. Moreover, by conducting polarization-dependent measurements, it is possible to identify the orbital character of bands based on matrix element effects<sup>107–109</sup> (Supplementary Information). Additionally, with a focusing system and tunable beam slit, a beam with a photon flux of  $\sim 10^{13}$  photons per second and a spot size of sub-100  $\mu\text{m}$  can routinely be achieved, thus facilitating ARPES measurements on small samples.

Despite these capabilities, synchrotron-based ARPES has its limitations. One main concern is the considerable construction and maintenance cost and effort required for synchrotron light sources, although synchrotrons are also important light sources for many experiments other than ARPES. Moreover, it remains a challenge to achieve both very high energy resolution (<1 meV) and high-flux synchrotron light, as the photon bandwidth can only be decreased at the expense of photon flux.

**Application to topological Weyl semimetals.** The continuously tunable VUV light with which most synchrotron-based ARPES set-ups are equipped has enabled many important breakthroughs in the study of topological materials, such as the observation of surface Fermi arcs in the Weyl semimetal TaAs (REFS<sup>37,91</sup>). Weyl semimetals<sup>33,34,37,88–95</sup> are a class of materials that can be regarded as 3D analogues of graphene wherein the bulk non-degenerate electronic bands disperse linearly along all momentum directions through a node near  $E_p$ , called a Weyl node, which can be viewed as a singular point of Berry curvature or a ‘magnetic monopole’ in momentum space<sup>123</sup>. Weyl nodes can appear in pairs of opposite chirality in a real material if the spin-doublet degeneracy of the bands is removed, which happens when either time-reversal or inversion symmetry is broken<sup>88–90,95</sup>. The low-energy excitations near the Weyl nodes behave like Weyl fermions, which were originally proposed by Hermann Weyl in 1929 as massless solutions of the Dirac equation<sup>124</sup>. However, Weyl fermions have not yet been observed in particle physics; hence, the physical realization of Weyl fermions in Weyl semimetals becomes more notable.

One hallmark of a Weyl semimetal is the existence of pairs of Fermi arcs at two opposite crystal surfaces. Each Fermi arc connects the projections of two opposite-chirality bulk Weyl nodes in the surface Brillouin zone<sup>88</sup>

(FIG. 2b). Synchrotron-based VUV ARPES, with its unique tunable light, has played a central part in identifying surface Fermi arcs in the TaAs family of semimetals (TaAs, TaP, NbAs and NbP). As an example, on performing photon-energy-dependent measurements along the  $\Gamma$ – $\bar{Y}$  direction in TaAs (FIG. 2c), the surface states at  $k_y \approx 0.4 \text{ \AA}^{-1}$  (where  $k_y$  is the momentum in the  $y$  direction) could be clearly identified as they do not show any noticeable change in  $k_x$  upon variation of the incident photon energy<sup>37</sup>. To identify the surface Fermi arcs, it is necessary to subsequently map out the Fermi surfaces by collecting photoelectrons of different emission angles. Indeed, a surface Fermi arc (labelled a5 in FIG. 2d) is clearly resolved in the Fermi surface map of TaAs and shows very good agreement with the calculated surface states on the (001) As-terminated surface<sup>91</sup> (FIG. 2e).

### Laser-based VUV ARPES

On the basis of their high photon flux and narrow bandwidth, lasers are a natural choice for laboratory-based ARPES. However, the photon energies generated by lasers are usually too low to overcome the 4–5 eV work function of metallic materials in an ARPES measurement. Great efforts have been made in recent years to develop high-energy (>5 eV) lasers that are suitable for ARPES, and by taking advantage of nonlinear optical processes, long-sought VUV lasers have been achieved<sup>119–25</sup>.

The VUV laser light required for the photoemission process is typically generated in one of two ways. One way is to exploit the process of harmonic generation through nonlinear optical crystals. The most commonly used nonlinear optical crystals are BaB<sub>2</sub>O<sub>4</sub> and KBe<sub>2</sub>BO<sub>3</sub>F<sub>2</sub>. Using BaB<sub>2</sub>O<sub>4</sub> crystals, a Ti:sapphire laser (with a photon wavelength and energy of  $\sim 800$  nm and 1.55 eV, respectively) with a sub-picosecond pulse width can output  $\sim 6$  eV laser light<sup>119</sup>, whereas with KBe<sub>2</sub>BO<sub>3</sub>F<sub>2</sub> crystals, a Nd:YVO<sub>3</sub> laser ( $\sim 1,064$  nm; 1.17 eV) with a femtosecond pulse width can produce  $\sim 7$  eV laser light with an ultranarrow bandwidth and a high flux<sup>21,22</sup>. Alternatively, VUV laser light can be generated using high harmonic generation (HHG) or multiphoton excitations in noble gases<sup>23,125–128</sup>; this approach generates laser light with a higher photon energy (approximately tens of eV) than that of nonlinear optical crystals (<10 eV). For example, a Yb-doped fibre laser,

when coupled with a xenon gas cell, can output  $\sim 11$  eV laser light<sup>23</sup>, and a Ti:sapphire laser with a gas cell can generate discretely tunable laser light in the range 15–40 eV with attosecond<sup>59</sup> or femtosecond pulse durations<sup>127</sup>. However, these sources usually have a relatively low photon flux ( $\leq 10^{13}$  photons per second) compared with 6–7 eV lasers, owing to the low generation efficiency of the HHG process and unavoidable loss of flux in the optics after generation. Moreover, the femtosecond or attosecond light pulses usually have a low energy resolution ( $\Delta E$ , of the order of tens of meV), which is constrained by the Fourier-transform limit. This limit, when expressed in terms of convenient units for Gaussian pulses with a pulse width  $\Delta\tau$ , is given by<sup>129</sup>

$$\Delta\tau\Delta E \geq 1,825 \text{ fsmeV} \quad (5)$$

where  $\Delta\tau$  and  $\Delta E$  are both quoted at full-width at half maximum. Although HHG laser light is not suitable for high-resolution ARPES measurements owing to the low energy resolution, the short pulse widths make it possible to perform time-resolved ARPES measurements at relatively high photon energies (discussed further below in the section on time-resolved ARPES).

Laser-based ARPES has many advantages. One major benefit of laser ARPES with low-energy ( $\sim 6$ – $7$  eV) photons is a substantial gain in the resolution of the in-plane momentum. From Eq. 2,

$$\Delta k_{\parallel}^f \propto \sqrt{2mE_{\text{kin}}/\hbar^2} \cdot \cos\theta \cdot \Delta\theta \quad (6)$$

Therefore, for the same  $\theta$  and  $\Delta\theta$ , photoelectrons with a low kinetic energy result in a better in-plane momentum resolution. Moreover, the high photon flux ( $\sim 10^{15}$  photons per second) and extremely narrow bandwidth ( $< 1$  meV) of some 6–7 eV laser light sources with long pulse widths ( $> 2$  ps) also make it possible to perform ARPES measurements with a very high energy resolution and with high data acquisition efficiency. Thus, the low-energy laser light sources have the advantage of ultrahigh energy and momentum resolution. Indeed, laser-based ARPES systems with a photon energy of  $\sim 7$  eV and energy resolution better than 1 meV have been achieved by using harmonic generation in a  $\text{KBe}_2\text{BO}_3\text{F}_2$  nonlinear crystal<sup>21,22</sup>. In addition, unlike noble-gas discharge lamps, it is easy to control the polarization of the laser light and to tune the beam spot size to the sub-100  $\mu\text{m}$  range. More importantly, pulsed laser light introduces a new degree of freedom to ARPES — time resolution — which we discuss in more detail below.

As with the other VUV light sources, laser light has its limitations. The main disadvantages are the limited tunability of the photon energy, low photoemission cross sections for some materials (for example, the cross section is  $< 0.01$  Mb per atom for Au with a 10 eV laser) and the inability to access electrons far from the centre of the Brillouin zone with a photon energy of 6–7 eV. To some extent, the application of HHG laser light with discretely tunable photon energies of tens of eV has overcome these problems. However, it remains difficult to obtain high-stability and high-flux photons with a narrow bandwidth.

**Application to  $\text{FeTe}_{0.55}\text{Se}_{0.45}$ .** To demonstrate the high-resolution power of laser-based ARPES, we highlight one application: the observation of a topological surface Dirac cone on the (001) surface of  $\text{FeTe}_{0.55}\text{Se}_{0.45}$  (REF.<sup>130</sup>). As the simplest iron-based superconductor (FIG. 3a),  $\text{Fe}(\text{Te},\text{Se})$  has attracted tremendous attention since its discovery in 2008 (REF.<sup>131</sup>). More recently, calculations<sup>132–134</sup> have predicted the existence of topological order in  $\text{FeTe}_{0.55}\text{Se}_{0.45}$ . The substitution of Se with Te lowers the energy of the  $p_z$  band and leads to band inversion in  $\text{FeTe}_{0.55}\text{Se}_{0.45}$  between the  $p_z(-)$  and  $d_{xz}(+)$  or  $d_{yz}(+)$  bands along the  $\Gamma$ –Z direction (FIG. 3b), where + and – denote even and odd parity under spatial inversion, respectively. Eventually, owing to the opening of the spin–orbit coupling gap between these two inverted bands, this material naturally hosts strong topological surface states inside the gap at the  $\bar{\Gamma}$  point of the (001) surface (FIG. 3c). The limited energy and momentum resolution of ARPES has, however, made it difficult to clearly resolve these surface states<sup>135,136</sup>. Only in 2018 were the Dirac surface states revealed through the use of high-resolution laser ARPES<sup>130</sup>. With this technique, a Dirac-cone surface state near  $E_F$  was clearly resolved from a high-resolution curvature intensity plot (FIG. 3d). More importantly, when  $\text{FeTe}_{0.55}\text{Se}_{0.45}$  enters the superconducting state, superconductivity is also induced in the topological surface states (FIG. 3e), and temperature-dependent and momentum-dependent measurements of the induced superconducting gap were recorded (FIG. 3f–h). The energy distribution curves at slightly higher temperatures show evidence of the hole branch of Bogoliubov quasiparticles (the shoulders above  $E_F$  in FIG. 3f), demonstrating the superconducting nature of the topological surface state. In addition, the superconducting gaps on the topological surface state are isotropic in momentum (FIG. 3g,h), which indicates that the surface state has an  $s$ -wave superconducting pairing symmetry. Therefore,  $\text{FeTe}_{0.55}\text{Se}_{0.45}$  provides an excellent platform for realizing Majorana zero modes based on the Fu–Kane model<sup>137</sup>, in which a single spin–momentum locked Dirac surface state with proximitized  $s$ -wave superconducting pairing can have the same role as a  $p$ -wave superconducting order parameter. Indeed, the Majorana zero modes have recently been observed in the superconducting vortex cores of  $\text{FeTe}_{0.55}\text{Se}_{0.45}$  with scanning tunnelling microscopy<sup>138</sup>.

### Bulk-sensitive soft-X-ray ARPES

Synchrotron-based VUV ARPES, usually with photon energies  $\geq 20$  eV, is an ideal tool for studying the surface electronic structure of many materials, especially topological materials. However, it is difficult to probe the bulk states of 3D materials with  $\geq 20$  eV VUV light owing to the extremely short escape depths of the resulting photoelectrons (FIG. 2a) and the ill-defined  $k_{\perp}$ . Although the photoelectrons ejected by 6–7 eV lasers have a longer escape depth (FIG. 2a) compared with those of  $\geq 20$  eV VUV sources, the non-tunable photon energy and stronger final-state effects<sup>69</sup> due to low-speed photoelectrons make it nearly impossible to probe the intrinsic 3D band structure of bulk states.

The only reliable way to examine 3D bulk states, especially the band dispersion along the  $k_{\perp}$  direction, is to use

**Bogoliubov quasiparticles**  
Elementary excitations of a Bardeen–Cooper–Schrieffer-type superconductor, corresponding to quantum superpositions of electrons and holes near the Fermi energy.

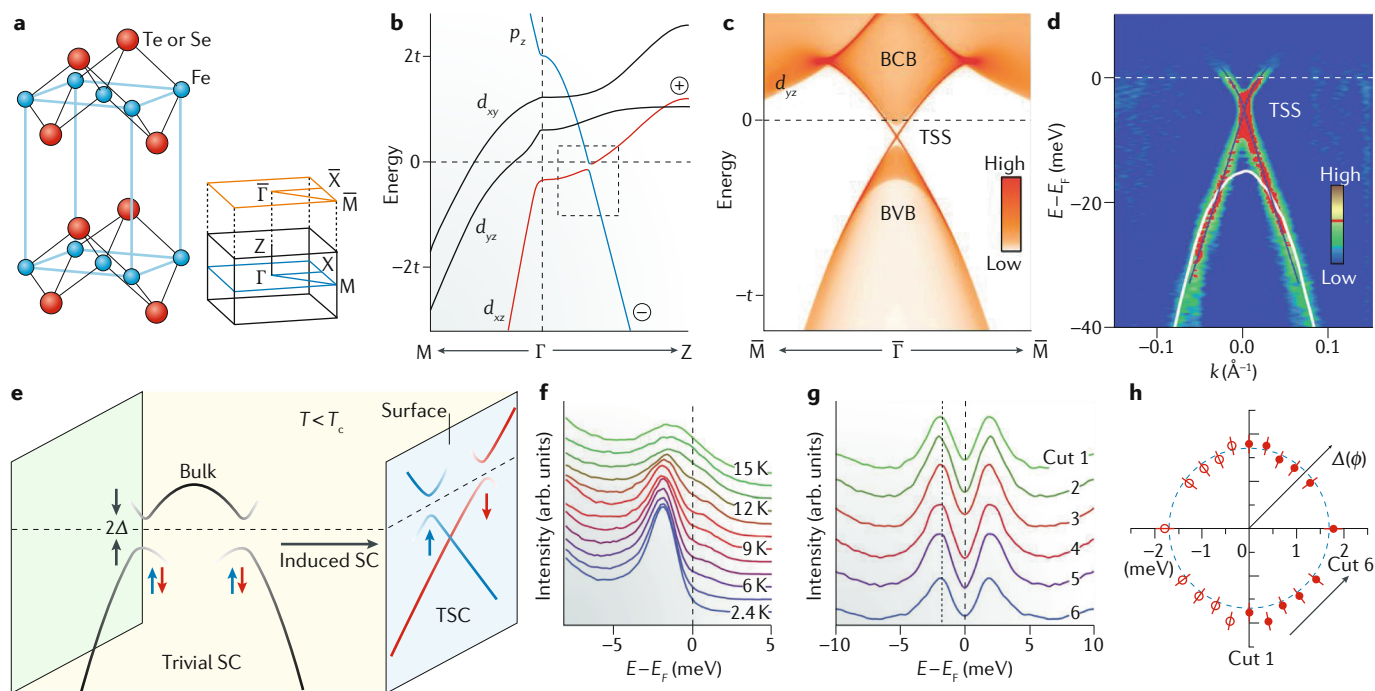


**Fig. 3 | Laser-based VUV ARPES measurements of a topological Dirac cone on the (001) surface of  $\text{FeTe}_{0.55}\text{Se}_{0.45}$ .** The high energy and momentum resolution of laser-based vacuum ultraviolet (VUV) angle-resolved photoemission spectroscopy (ARPES) has enabled the identification of the Dirac surface states in  $\text{FeTe}_{0.55}\text{Se}_{0.45}$ . **a** | Crystal structure (left) and the bulk and projected (001) surface Brillouin zones (right) of  $\text{Fe}(\text{Te},\text{Se})$ . **b** | Calculated band structure of  $\text{FeTe}_{0.55}\text{Se}_{0.45}$  along the  $\Gamma$ -M and  $\Gamma$ -Z directions (where  $t = 100$  meV). The dashed box shows the spin-orbit coupling gap of the inverted bands. **c, d** | Calculated band structure (panel **c**;  $t = 100$  meV) and curvature intensity plot of ARPES data (panel **d**) along the  $\Gamma$ -M direction (where  $k$  is the momentum in the  $\Gamma$ -M direction). The topological surface states (TSSs) connecting the bulk valence band (BVB) and bulk conduction band (BCB) are clearly resolved in both images. The ARPES data in panel **d** were recorded with a  $p$ -polarized 7 eV laser at 15 K. **e** | Schematic of the bulk and surface superconducting (SC) states in  $\text{FeTe}_{0.55}\text{Se}_{0.45}$ . Below the superconducting transition temperature ( $T_c$ ), the bulk states open  $s$ -wave SC gaps (where  $\Delta$  is the SC gap size); these bulk states are topologically trivial because of their spin degeneracy (black curves). Owing to the superconducting proximity effect, the TSS also opens an isotropic gap at temperatures ( $T < T_c$ ) and is topologically superconducting (TSC) as a consequence of the spin polarization (blue and red curves). **f** | Raw energy-distribution curves measured at different temperatures for a  $k$  point on the Fermi surface. The shoulders above the Fermi level ( $E_f$ ) signify SC Bogoliubov quasiparticles. The energy positions of the coherence peaks in the energy-distribution curves correspond to the SC gap size. **g** | Symmetrized energy-distribution curves of the Dirac surface states at different Fermi wavevectors (indicated in panel **h**) recorded at  $T = 2.4$  K. **h** | Polar representation of the measured SC gap size in panel **g**. The measured SC gaps (solid markers) at different polar angles ( $\phi$ ) almost have the same value, demonstrating that the SC gaps of surface states are also isotropic in momentum. The hollow markers are a mirror reflection of the solid markers, and the vertical lines passing through the solid or hollow markers indicate the error bars.  $E$ , energy. Adapted with permission from REF.<sup>130</sup>, AAAS.

higher photon energies in the soft-X-ray regime<sup>12,16,30–32</sup>. There are three main reasons that soft-X-ray ARPES facilitates the study of bulk states. First, the higher kinetic energy of the photoelectrons ejected by soft X-rays results in an increase in the photoelectron escape depth by a factor of 2–4 compared with that of 20 eV VUV light (for which the escape depth is  $\sim 5$  Å); this increase greatly enhances the sensitivity to the bulk electronic states. Second, from the Heisenberg uncertainty principle, the momentum broadening of photoelectrons along the  $k_{\perp}$  direction,  $\Delta k_{\perp}$ , is given by  $\Delta k_{\perp} \propto d^{-1}$ , where  $d$  is the photoelectron escape depth. Thus, an increase in the escape depth with soft X-rays leads to a decrease of  $\Delta k_{\perp}$  and an improvement in the  $k_{\perp}$  resolution, which enables accurate investigations of the bulk states of 3D materials in the entire momentum space. Third, in the photoemission process with high-energy soft-X-ray

incident light, the final states are truly free-electron-like, which enables precise determination of the  $k_{\perp}$  value from Eq. 3.

In addition to the high sensitivity to bulk electronic states, soft-X-ray ARPES has other advantages, such as simplified matrix elements and, compared with VUV ARPES, a lower sensitivity to the sample surface quality. However, soft-X-ray ARPES also suffers from several problems. The main difficulty is a decrease in the valence-band cross section by two to three orders of magnitude compared with the VUV energy range<sup>119</sup>. This decrease is due to reduced wavefunction overlap between the spatially rapidly varying final states and the spatially smooth valence states. Thus, only initial electronic states near a very small region around the ion core, the wavevector of which matches the large wavevector of the high-energy final states, contribute significantly

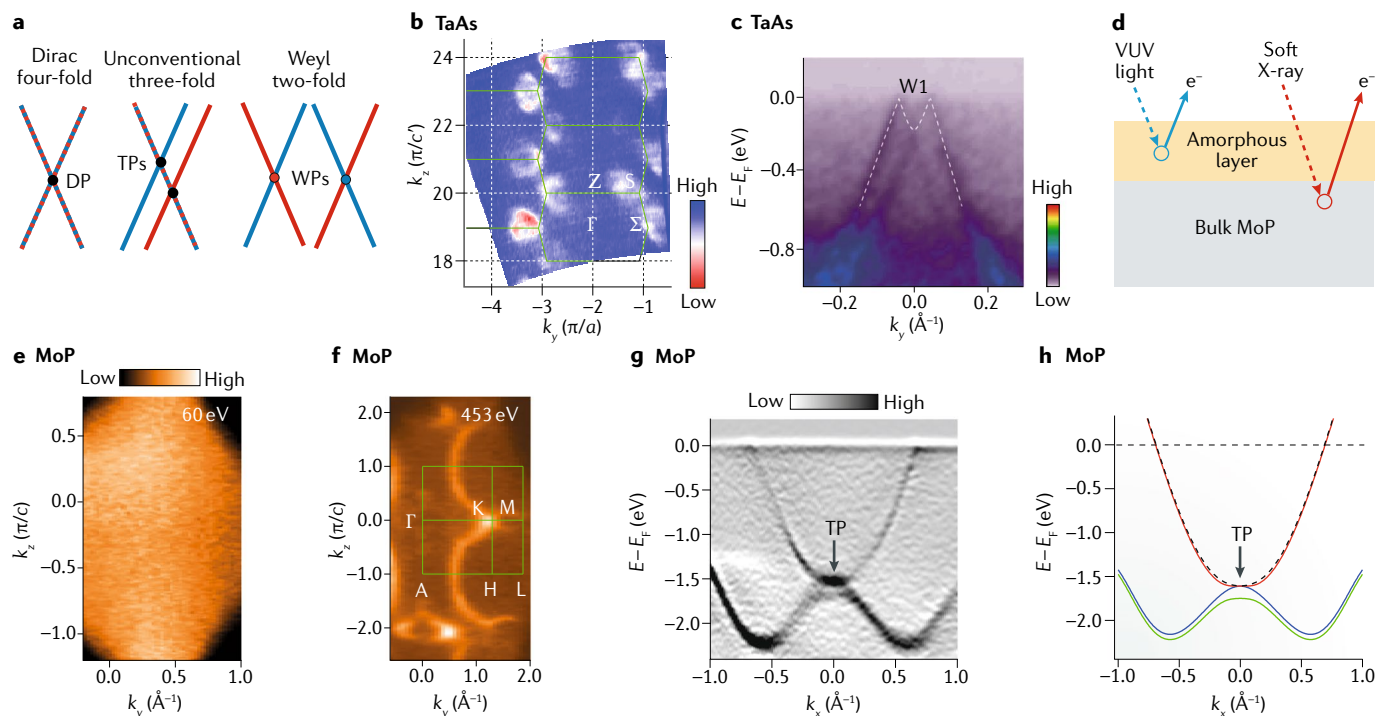


**Fig. 4 | Soft-X-ray ARPES studies of the bulk electronic structure of TaAs and MoP.** Soft-X-ray angle-resolved photoemission spectroscopy (ARPES) is a bulk-sensitive technique that has been used to identify Weyl points and triple points in the bulk electronic structure of TaAs and MoP, respectively. **a** | Schematic of a Dirac fermion, an unconventional three-component fermion and a Weyl fermion, which have band-crossing points with four-fold (Dirac point, DP), three-fold (triple degenerate point, TP) and two-fold (Weyl point, WP) degeneracies, respectively. Bands shown in a single colour (red or blue) are non-degenerate, and bands with mixed colours are doubly degenerate. **b** | ARPES intensity plot of TaAs at the Fermi level ( $E_F$ ) in the  $k_y$ - $k_z$  plane at  $k_x=0$  (where  $k_x$ ,  $k_y$  and  $k_z$  are the momenta in the  $x$ ,  $y$  and  $z$  directions, respectively). The green lines indicate the Brillouin-zone boundaries in the  $k_y$ - $k_z$  plane.  $c'$  is one-half of the  $c$ -axis lattice constant of TaAs. **c** | ARPES intensity plot showing the experimental M-shaped band dispersions of one pair of Weyl points (W1) in TaAs. **d** | Schematic showing the photoemission process with bulk-sensitive soft X-rays and surface-sensitive vacuum ultraviolet (VUV) light on the (100) cleaved surface of an MoP single crystal covered by an amorphous layer. **e,f** | ARPES intensity maps in the  $k_z=0$  plane at  $E_F$  recorded on the same (100) cleaved surface of MoP with VUV (60 eV; panel **e**) and soft-X-ray (453 eV; panel **f**) light. **g,h** | Curvature intensity plot of ARPES data (panel **g**) and calculated band structure (panel **h**; the four lines represent four spin non-degenerate bands) along the  $k_x$  direction at  $k_z=0.75\pi$  (which corresponds to the TP in MoP).  $E$ , energy. Panels **a** and **f-h** are adapted from REF.<sup>35</sup>, Springer Nature Limited. Panel **b** is adapted from REF.<sup>33</sup>, Springer Nature Limited. Panel **c** is adapted from REF.<sup>150</sup>, Springer Nature Limited.

to the photoemission intensity<sup>139,140</sup>. This signal loss can be compensated by a high flux of incident photons. For example, owing to the advances in synchrotron radiation sources and beamline instrumentation, the soft-X-ray ARPES end-station at the Swiss Light Source has successfully compensated the signal loss with a soft-X-ray flux of  $>10^{13}$  photons per second<sup>16</sup>.

Another difficulty with soft-X-ray ARPES, in sharp contrast to low-energy laser ARPES, is that the use of high-energy soft-X-rays leads to a reduction in the in-plane momentum resolution (Eq. 6). Therefore, spectrometers need to be equipped with a higher angular resolution to improve the  $k_{\parallel}$  resolution. Furthermore, compared with VUV ARPES, soft-X-ray ARPES also suffers from a loss of energy resolution. More specifically, the energy resolution of VUV ARPES can be better than 1 meV, whereas for soft-X-ray ARPES, the energy resolution varies from tens of meV to 100 meV depending on the photon energy. Finally, we caution that the photon momentum of soft X-rays ( $\sim 0.25 \text{ \AA}^{-1}$  at 500 eV) may not be negligible compared with the typical size of

the Brillouin zone ( $\sim 1\text{--}2.5 \text{ \AA}^{-1}$ ). Hence, the momentum conservation law in Eq. 2 may no longer hold.

#### Application to topological semimetals

To illustrate the study of bulk electronic structure using soft-X-ray ARPES, and to demonstrate how central the improvement in  $k_{\perp}$  resolution has been in this regard, we use 3D topological semimetals TaAs (REFS<sup>33,34</sup>) and MoP (REF.<sup>35</sup>) as examples. Topological semimetals, which have symmetry-protected band-crossing points, have become one of the most intensively studied fields in condensed matter physics. The most famous examples are Dirac<sup>83–87</sup> and Weyl semimetals<sup>33,34,37,88–95</sup>, in which two doubly or singly degenerate bands cross, forming four-fold Dirac points or two-fold Weyl points, respectively (FIG. 4a). New types of crystal symmetry-protected band crossings have been theoretically predicted in condensed matter systems, and the corresponding low-energy excitations have no high-energy counterparts<sup>141–149</sup>. These excitations, also referred to as unconventional fermions, could challenge our existing wisdom

about the classification and properties of fermions. For example, topological semimetals with three-fold band crossings have been predicted in several materials with WC-type structures<sup>144–146</sup>. The quasiparticle excitations near the band-crossing points are three-component fermions, which can be viewed as the intermediate species between the four-component Dirac and two-component Weyl fermions.

With the ability to probe more deeply into a sample, soft-X-ray ARPES has had a key role in the detection of bulk Weyl points in TaAs (REFS<sup>33,34</sup>) and triply degenerate points in MoP (REF.<sup>35</sup>) and WC (REF.<sup>36</sup>). For the Weyl semimetal TaAs, first-principles calculations indicated that there are 12 pairs of Weyl points in the bulk Brillouin zone<sup>95</sup>. However, owing to the short escape depth of the photoelectrons excited by VUV light, the bulk Weyl points could not be resolved in VUV ARPES experiments<sup>91</sup> (FIG. 2d). However, with soft-X-ray ARPES, the bulk Weyl bands are clearly resolved<sup>33,34,150</sup>. The measured electronic states in the  $\Gamma$ - $\Sigma$ - $Z$ - $S$  plane, which is perpendicular to the cleaved sample surface, clearly exhibit a periodic modulation upon varying the incident soft-X-ray photon energy (hence varying  $k_{\parallel}$ ; FIG. 4b), confirming the bulk nature of the detected spectra. The bulk Weyl points (labelled W1 in FIG. 4c) were confirmed from the measured M-shaped band dispersion, with the two peaks corresponding to a pair of Weyl points of opposite chirality.

The benefits of soft-X-ray ARPES are further illustrated in studies on MoP (REF.<sup>35</sup>). Owing to its 3D crystal structure, the top layer of the cleaved surface of MoP is amorphous (FIG. 4d). Therefore, with VUV ARPES, no obvious Fermi surface is observed at 60 eV (FIG. 4e) owing to a combination of the limited detection depth of VUV ARPES and the angle-smearing effect of scattering in the amorphous layer. However, upon increasing the photon energy to 453 eV, the bulk states are clearly seen (FIG. 4f), enabling the detection of the predicted triply degenerate point. Indeed, by using high-precision measurements of the band dispersions, it is possible to resolve the triply degenerate point with soft X-rays (FIG. 4g), and this is well reproduced by calculations (FIG. 4h).

### Spin-resolved ARPES

Historically, the development of ARPES has been driven by the demands of research for a specific class of materials. For example, the discovery of the high- $T_c$  superconductors promoted the development of high-resolution laser ARPES<sup>21,22</sup>. Similarly, the recent discovery of topological insulators and non-centrosymmetric materials has stimulated the development of high-performance spin-resolved ARPES<sup>38–42</sup>.

The integration of spin detectors into ARPES spectrometers enables spin-resolved ARPES, and substantial efforts have been made to develop compact spin polarimeters. Examples of detectors include those using spin-polarized low-energy electron diffraction<sup>151</sup>, diffuse scattering<sup>152</sup>, Mott scattering<sup>39</sup> and very low-energy electron diffraction (VLEED)<sup>153</sup>. Most of these spin detectors are based on the asymmetry ( $A_m$ ) of preferential spin scattering, which can be written as  $A_m = (I_+ - I_-)/(I_+ + I_-)$ , where  $I_+$  and  $I_-$  are the partial intensities of electrons

with magnetic moments parallel or antiparallel, respectively, to the target magnetization direction of the detector. The final spin polarization ( $P$ ) is proportional to the asymmetry:  $P = A_m/S_f$ , where  $S_f$  is the spin sensitivity (a coefficient called the Sherman function in Mott detectors), which can be determined by measuring a fully polarized electron beam with  $A_m = 1$ . The most widely used spin polarimeters are Mott detectors<sup>39</sup> and VLEED detectors<sup>153</sup>, which use heavy elements (such as Au and Th) and ferromagnetic thin films (such as Fe(001) and Co(001) films) as scattering targets, respectively. A Mott detector uses the scattering asymmetry induced by the spin-orbit interaction when high-energy ( $\sim 20$ – $100$  keV) electrons scatter off a heavy-element target. By contrast, a VLEED detector takes advantage of the exchange scattering asymmetry of very low-energy ( $< 10$  eV) electrons with ferromagnetic thin films. Mott detectors have the advantage of using scattering targets with long lifetimes, but the scattering rate ( $\sim 10^{-4}$ ) is very low owing to the low cross sections of the high-kinetic-energy electrons. By contrast, VLEED detectors have a much higher efficiency (approximately two orders of magnitude higher than that of Mott detectors), owing to the higher scattering probability of very low-energy electrons and improved spin sensitivity. However, the ferromagnetic thin-film target has to be regenerated frequently, typically once every few weeks, because of degradation of the thin film.

Spin-resolved ARPES is one of the most powerful techniques for directly measuring the spin texture of electronic states. However, it also has several shortcomings. First, the energy resolution and angular resolution of the detectors still lag behind those of non-spin-resolved electron analysers. Second, the detectors have a low efficiency, which is due to the small scattering cross section and the single detection channel, in which only photoelectrons emitted within a small solid angle are recorded. Notably, recent advances in spin detectors<sup>154–160</sup> and light sources have greatly improved the performance of spin-resolved ARPES. For example, combining a state-of-the-art spin detector (a Scienta Omicron DA30-L spin spectrometer; FIG. 5a) and a high-photon-flux VUV laser, a high efficiency spin-resolved ARPES system with an energy resolution of 1.7 meV was achieved<sup>40</sup>. The DA30-L spin spectrometer combines a hemispherical electron analyser with twin VLEED spin detectors (VLEED-B and VLEED-W). The electron analyser is equipped with electron deflectors, whereby an applied electric field is used to select photoelectrons of desired emission angles. The DA30-L analyser therefore enables detailed  $k$ -space mapping of 2D in-plane electronic structure,  $E(k_x, k_y)$ , at a fixed sample geometry with acceptance angles  $\theta_x = 30^\circ$  and  $\theta_y = 24^\circ$ , where  $x$  and  $y$  are the directions parallel and perpendicular to the entrance slit, respectively. The twin VLEED spin detectors use oxidized iron films as scattering targets, and the film target of VLEED-B (VLEED-W) is magnetized by solenoid coils in the  $x$  and  $z$  ( $y$  and  $z$ ) directions, which correspond to the spin-polarization directions of  $P_x$  and  $P_z$  ( $P_y$  and  $P_z$ ) on the sample axis. Thus, the DA30-L spin spectrometer enables analysis of the 3D spin vector of photoelectrons emitted in the acceptance cone

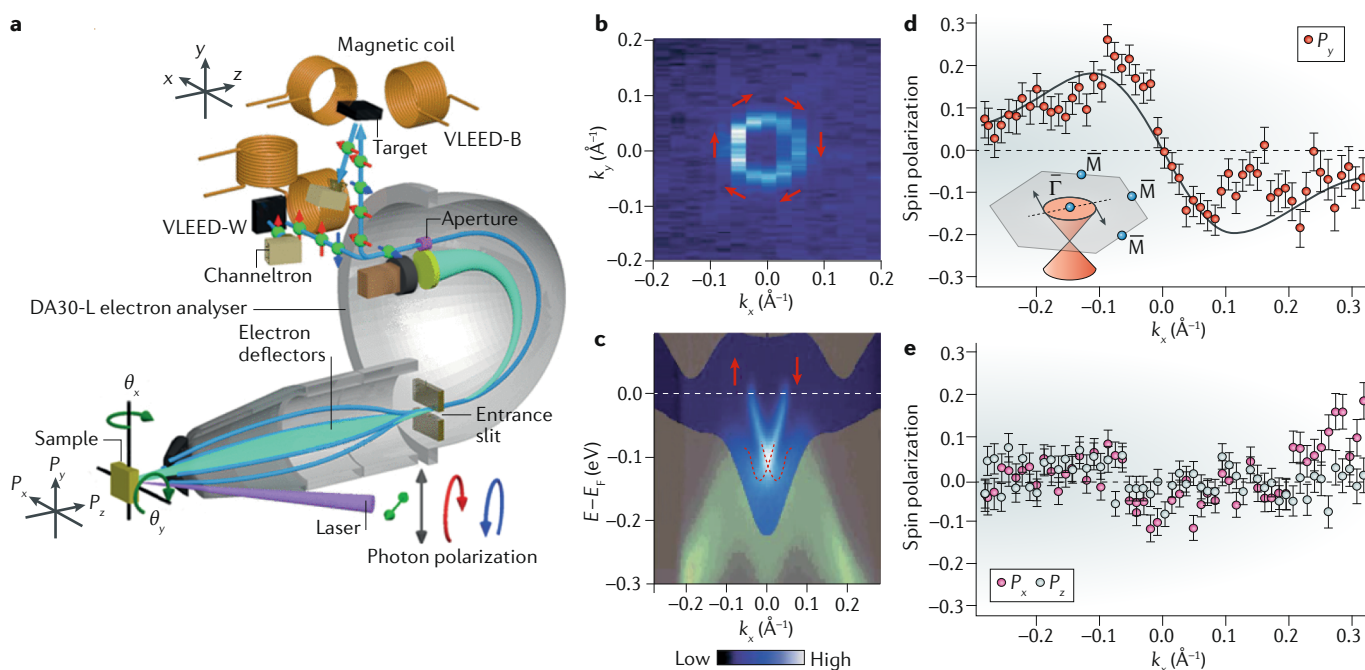


**Fig. 5 | Spin-resolved ARPES in the study of the spin texture of electronic states in  $\text{Bi}_2\text{Te}_3$ .** Spin-resolved angle-resolved photoemission spectroscopy (ARPES) is a powerful tool for probing the spin texture of the electronic states of topological insulators, such as  $\text{Bi}_2\text{Te}_3$ . **a** | Schematic of a spin-resolved ARPES system<sup>40</sup>. In this example, two very low-energy electron diffraction (VLEED) spin detectors (VLEED-B and VLEED-W) are arranged orthogonally with respect to each other and are connected to the end of a DA30-L hemispherical electron analyser.  $\theta_x$  and  $\theta_y$  are the polar and tilt angles of sample, respectively. **b** | ARPES intensity map at the Fermi level ( $E_F$ ) recorded on the (111) cleaved surface of  $\text{Bi}_2\text{Te}_3$ . The red arrows denote the direction of spin projection onto the  $k_x$ - $k_y$  plane (where  $k_x$  and  $k_y$  are the momenta in the  $x$  and  $y$  directions, respectively) around the Fermi surface. **c** | ARPES intensity plot along the  $k_x$  ( $\bar{\Gamma}$ - $\bar{M}$ ) direction. The dotted red lines indicate the Dirac cone, and the red arrows indicate the spin texture. The shaded regions are the calculated projections of the bulk bands onto the (111) surface. **d** | Plot of the measured  $y$  component of the spin polarization ( $P_y$ ) along the  $\bar{\Gamma}$ - $\bar{M}$  direction at a binding energy of  $-20$  meV, which only cuts through the surface states. The black solid line is a numerical fit, and the inset shows a schematic of the cut direction and the corresponding spin texture of the Dirac-cone surface state. **e** | Plot of the measured  $x$  and  $z$  components of the spin polarization ( $P_x$  and  $P_z$ , respectively) along the  $\bar{\Gamma}$ - $\bar{M}$  direction. The error bars in panels **d** and **e** represent the standard deviation of  $P_x$ ,  $P_y$  and  $P_z$ .  $E$ , energy. Panel **a** is adapted from REF.<sup>40</sup>, with the permission of AIP Publishing. Panels **b**-**e** are adapted from REF.<sup>43</sup>, Springer Nature Limited.

of  $(\theta_x \times \theta_y) = (30^\circ \times 24^\circ)$  without sample rotation. Note, however, that, in general, the spin-polarization signal can be complicated by matrix element effects<sup>161-163</sup>. Thus, photon-energy-dependent and photon-polarization-dependent spin-resolved ARPES measurements are needed to check whether the spin signal is intrinsic to the magnetic moment of the photoelectrons<sup>45,46</sup>.

#### Application to 3D topological insulators

The discovery of 3D topological insulators has helped to drive the development of spin-resolved ARPES. A topological insulator is a state of quantum matter that features an energy gap in the bulk but gapless Dirac-cone surface states that reside inside the bulk insulating gap<sup>43,44,72,75-77</sup>. The distinctive feature of a Dirac-cone surface state is the spin-momentum locking pattern<sup>76</sup>, which manifests as a spin texture that winds in a circle around a constant-energy contour of the Dirac-cone surface state (FIG. 5b). To highlight the role of spin-resolved ARPES in the examination of the spin texture of these surface states, we use  $\text{Bi}_2\text{Te}_3$  as an example because it hosts a clean Dirac cone near  $E_F$  (FIG. 5c). Indeed, the spin-momentum locking feature of the surface electrons

in  $\text{Bi}_2\text{Te}_3$  was observed with spin-resolved ARPES<sup>43</sup>. The measured spin-polarization spectra along  $\bar{\Gamma}$ - $\bar{M}$  in the  $x$ ,  $y$  and  $z$  directions (FIG. 5d,e) show that there is no clear spin polarization in the  $x$  and  $z$  directions within the experimental resolution, whereas clear polarization signals of equal magnitude and opposite signs are observed in the  $y$  direction. This finding implies that the surface electrons of opposite momenta also have opposite spin textures, confirming the spin-momentum-locking scenario. Besides spin-resolved ARPES, the spin textures of electronic states can also be extracted from the spin-dependent differential absorption of left-circularly versus right-circularly polarized light, which is the basis of circular dichroism<sup>164-166</sup>.

#### Ultrafast time-resolved ARPES

Non-time-resolved ARPES serves as an excellent tool for probing the band dispersion of equilibrium states. However, it remains challenging to distinguish and quantify many-body interactions (for example, electron-electron and electron-phonon interactions) of correlated materials. Generally, electron-electron, electron-spin and electron-phonon interactions occur

on timescales of femtoseconds, tens of femtoseconds and picoseconds<sup>167–169</sup>, respectively. Therefore, the use of sub-picosecond or even sub-femtosecond laser pulses in pump–probe experiments enables the coupled interactions between the charge, spin, lattice and orbital degrees of freedom to be disentangled<sup>170</sup>. In particular, the combination of pump–probe optical spectroscopy with ARPES, namely time-resolved ARPES<sup>20,55–59</sup>, provides direct insight into the energy and momentum dependence of these ultrafast dynamics.

In a time-resolved ARPES experiment (FIG. 6a), a femtosecond laser pulse (the ‘pump’) is used to perturb a material into a non-equilibrium state. Subsequently, a second time-delayed pulse (the ‘probe’), which is typically in the VUV range, is used to excite photoelectrons out of the sample; these photoelectrons are then analysed by an electron spectrometer. By varying the time delay between the pump and probe pulses, it is possible to obtain insight into the time-dependent processes involved in the excitation and relaxation of the transient states. Besides providing energy-resolved and momentum-resolved transient spectra in the time domain<sup>60–68</sup>, time-resolved ARPES also allows for the investigation of unoccupied states above  $E_F$  by populating them with photoexcited electrons while keeping the band structure minimally disturbed<sup>69–71</sup>. It is worth mentioning that besides time-resolved ARPES, the unoccupied states can also be detected using two-photon photoemission spectroscopy<sup>167–169,171–175</sup> (see Supplementary Information for further details).

Typically, the probe photon source is a femtosecond VUV laser pulse generated from nonlinear crystals or noble gases. For the pump pulse, frequencies that range from visible light down to terahertz light<sup>67</sup> are applicable; among these, the most commonly used photon energy is  $\sim 1.55$  eV (which is the fundamental frequency of the popular femtosecond solid-state laser based on Ti-doped sapphire crystals). The limitations of VUV laser ARPES were discussed above. In addition to these limitations, femtosecond pulses constrain the energy resolution owing to the Fourier-transform limit (Eq. 5). For example, a 150 fs laser pulse cannot achieve an energy resolution better than 12 meV, whereas a 10 ps laser has achieved an energy resolution of 0.26 meV (REFS<sup>21,22</sup>). Another drawback of time-resolved ARPES is the low detection efficiency relative to non-time-resolved VUV ARPES, owing to the low intensity of the laser pulses, which are constrained by the space-charge effect because photoelectrons are generated within a small region in space and in time<sup>122</sup>. Consequently, a laser source with a high repetition rate ( $\geq 10$  kHz) is necessary to increase the overall photoelectron count while minimizing the space-charge effects by reducing the count per pulse.

To achieve higher angular resolution and efficiency, the angle-resolved time-of-flight (ARTOF) analyser has been developed<sup>11,166</sup>. A typical ARTOF analyser (for example, the **ARTOF-2 analyser** from Scienta Omicron) comprises several cylindrical electrostatic lenses with a defined angular acceptance. These lenses image the emitted electrons onto a position-sensitive delay-line detector located at the end of the series of lenses. The kinetic energy and emission angle of a photoelectron can be

obtained from a combination of its flight time from the sample to the detector and the position at which it strikes the detector. This delay-line detector enables energy and momentum data to be collected for a complete area of the Brillouin zone ( $E(k_x, k_y)$ ) rather than along a specific line  $E(k_x)$ , as with a traditional hemispherical analyser<sup>9</sup>. The ARTOF analyser can therefore collect photoelectrons from a complete emission cone within the angular acceptance, whereas a traditional hemispherical analyser can only collect photoelectrons from a specific emission plane. Thus, with an ARTOF analyser, a higher detection efficiency is achieved. However, traditional ARTOF analysers (such as ARTOF-2) can detect at most one electron per pulse because the delay-line detector can only recognize single electron strokes. New types of delay-line detectors have therefore been developed (such as the **RoentDek delay-line detectors**) to overcome this limitation by enabling multiple electrons to be detected simultaneously per pulse. The relatively high efficiency of ARTOF analysers makes them ideal detectors for pulsed lasers. However, the inherent requirement for the pulsed beams to have repetition rates  $< 3$  MHz, for compatibility with the delay-line detectors, prohibits the application of ARTOF analysers to light sources that have repetition rates  $> 3$  MHz, including most synchrotron light sources, gas-discharge lamps and quasi-continuous lasers. Another drawback of ARTOF analysers is the high background noise of scattered photons off the sample surface, which travel in a straight line to the delay-line detector. By contrast, scattered photons are not an issue for hemispherical detectors because the scattered photons are either blocked by the narrow entrance slit at one end of the hemisphere or stopped in the curved hemisphere if a small fraction passes the slit, and thus do not reach the detector at the opposite end of the hemisphere.

The rapid development of commercially available, high-repetition-rate ( $\geq 10$  kHz), amplified femtosecond lasers has led to the increased use of time-resolved ARPES. In the past 10 years, various time-resolved ARPES systems<sup>55,57,125–127,176–180</sup> with different energy resolution (tens to hundreds of meV), temporal resolution (approximately hundreds of attoseconds<sup>58,59</sup> to hundreds of femtoseconds) and pump frequencies (approximately tens of meV to several eV) have been developed, enabling the electron dynamics in correlated materials to be probed. Moreover, by carefully choosing the pump frequency, it is possible to observe new quantum states induced by light, such as Floquet–Bloch states<sup>64,181,182</sup> (discussed below).

#### Application to grey As and Bi<sub>2</sub>Se<sub>3</sub>

The capability of time-resolved ARPES as a tool to directly probe the dynamics of transient states and unoccupied states is clearly illustrated in the study of grey As (REF.<sup>70</sup>). Grey As exhibits non-trivial Rashba-split Shockley states on the (111) surface; these non-trivial states arise from a bulk band inversion caused by the crystal field. To elucidate the non-trivial band topology of these Shockley states, time-resolved ARPES measurements were performed on the (111) surface to probe the unoccupied states above  $E_F$ . The ARPES

#### Delay-line detector

A position-sensitive detector that can determine the position of the signal source by measuring the difference in the signal arrival times at different ends of the delay line.

#### Shockley states

Interfacial electronic states that arise from the abrupt change in electric potential on the crystal surface or at the boundary of two materials.

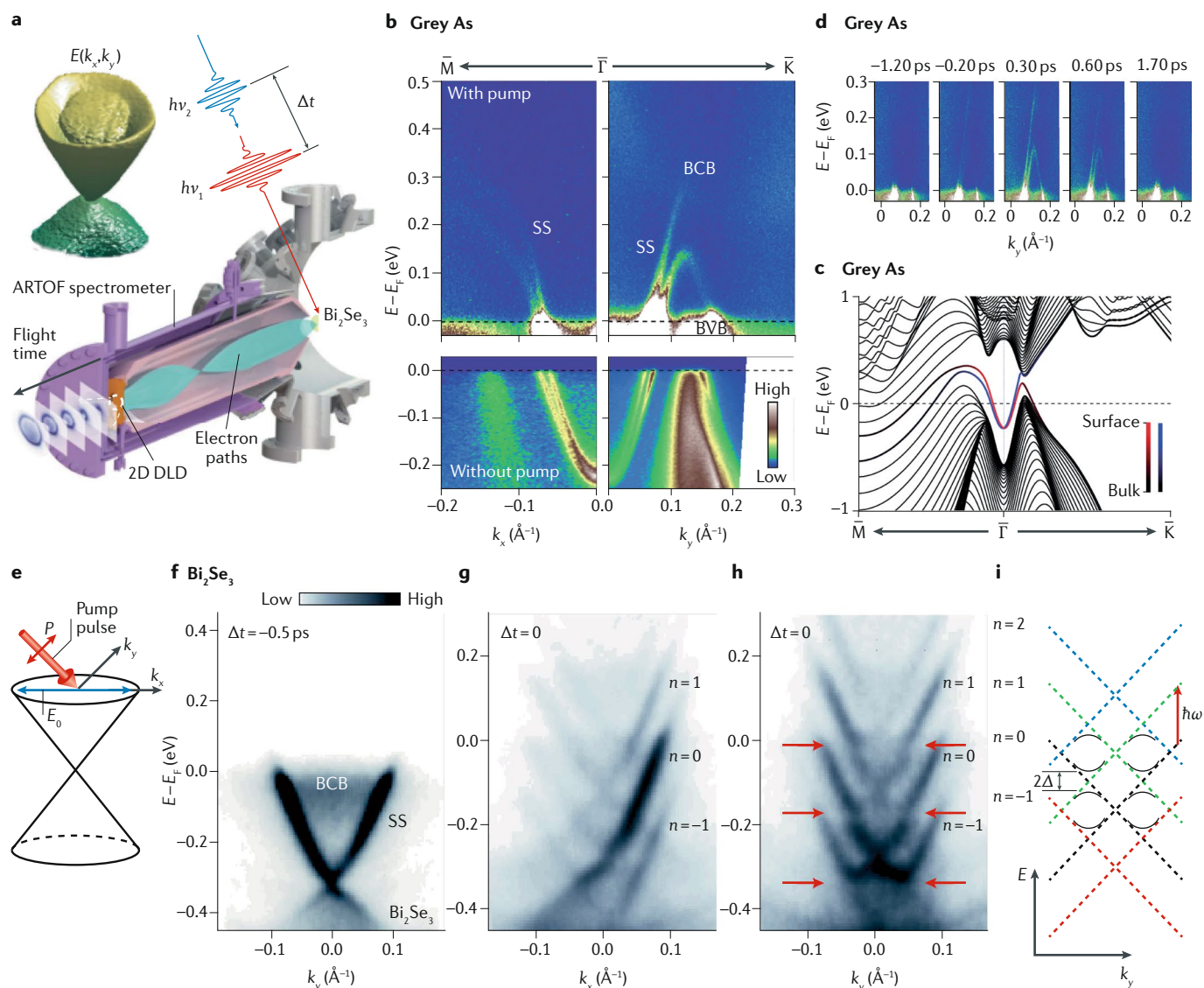


**Fig. 6 | Time-resolved ARPES studies of grey As and  $\text{Bi}_2\text{Se}_3$ .** Time-resolved angle-resolved photoemission spectroscopy (ARPES) can be used to probe the dynamics of transient states and to manipulate the electronic structure of a material. **a** | Schematic of a time-resolved ARPES system with an angle-resolved time-of-flight (ARTOF) spectrometer<sup>166</sup>. In this set-up, a pump laser with photon energy  $h\nu_1$  is used to excite a material into a non-equilibrium state. Subsequently, a probe laser pulse with photon energy  $h\nu_2$ , arriving after a time delay  $\Delta t$ , is used to eject photoelectrons from the sample. The photoelectrons are then analysed by an ARTOF detector, which calculates the electron kinetic energy by measuring the flight time from the sample to the detector and deduces the electron momentum from the strike position on the 2D delay-line detector (DLD). An ARTOF analyser can therefore measure the entire band structure  $E(k_x, k_y)$  (where  $E$  is the energy, and  $k_x$  and  $k_y$  are the momenta in the  $x$  and  $y$  directions, respectively) simultaneously; an example is shown for the surface Dirac cone in  $\text{Bi}_2\text{Se}_3$  (top left). **b** | Measured band dispersions of grey As on the (111) surface above and below the Fermi level ( $E_F$ ) along the  $\bar{M}-\bar{\Gamma}-\bar{K}$  direction. The top parts show the band dispersions above  $E_F$  recorded using time-resolved ARPES measurements. The bottom parts show the band dispersions below  $E_F$  recorded using high-resolution static laser ARPES measurements. **c** | Slab calculations of surface bands with opposite spin orientations (shown in red and blue) of the (111) surface of grey As and the bulk bands (indicated in black) along the  $\bar{M}-\bar{\Gamma}-\bar{K}$  direction. **d** | Time-resolved ARPES intensity snapshots of grey As along the  $\bar{\Gamma}-\bar{K}$  direction with various pump-probe delay times. The snapshots show the excitation or decay process of the electronic states above  $E_F$ . **e** | Illustration showing the experimental geometry of a time-resolved ARPES measurement with a  $p$ -polarized pump laser. The cone structure represents the surface Dirac cone (centred at the  $\Gamma$  point) of  $\text{Bi}_2\text{Se}_3$ . The double-headed red arrow indicates the linear polarization ( $P$ ) of the pump laser, and the blue arrow denotes the electric field ( $E_0$ ) of the pump laser projected onto the sample surface. **f** | Time-resolved ARPES intensity plot of  $\text{Bi}_2\text{Se}_3$  along the  $k_y$  direction at  $\Delta t = -0.5$  ps with a  $p$ -polarized pump laser. **g, h** | Time-resolved ARPES intensity plots of  $\text{Bi}_2\text{Se}_3$  along the  $k_x$  (panel **g**) and  $k_y$  (panel **h**) directions at  $\Delta t = 0$  with a  $p$ -polarized mid-infrared pump laser. The red arrows in panel **h** indicate the avoided crossing gaps.  $n$  indicates the order of the Floquet-Bloch bands. **i** | Sketch of the 'dressed' replica bands of different orders induced by the mid-infrared pump pulse. Avoided crossings occur along the  $k_y$  direction, leading to a bandgap of  $2\Delta$ . BCB, bulk conduction band; BVB, bulk valence band;  $E$ , energy;  $h\omega$ , photon energy of pump pulse; SS, surface state. Panel **a** is adapted with permission from REF.<sup>166</sup>, APS. Panels **b-d** are adapted with permission from REF.<sup>70</sup>, APS. Panels **f-h** are adapted from REF.<sup>182</sup>, Springer Nature Limited. Panel **i** is adapted with permission from REF.<sup>64</sup>, AAAS.

data (FIG. 6b) clearly reveal a pair of parabolic bands, which split along both the  $\bar{\Gamma}$ – $\bar{M}$  and  $\bar{\Gamma}$ – $\bar{K}$  directions but are degenerate at the  $\bar{\Gamma}$  point. In the  $\bar{\Gamma}$ – $\bar{K}$  direction, one band disperses into the conduction band, while the other turns back and merges into the valence band. This behaviour shows excellent agreement with the calculated band structure (FIG. 6c), thus providing strong evidence for the non-trivial band topology of the Shockley states. Furthermore, by varying the pump–probe delay time, the dynamics of these unoccupied states, such as the characteristic relaxation time, can be revealed (FIG. 6d).

Time-resolved ARPES can also be used to detect new quantum states that emerge from the coherent interaction between electrons and photons. Among the most intriguing achievements has been the observation of Floquet–Bloch states<sup>64,181,182</sup> in  $\text{Bi}_2\text{Se}_3$ . According to Bloch's theorem, a spatially periodic potential in a lattice results in the replication of band dispersion in momentum, namely, Bloch states. In analogy to Bloch states, a temporally periodic electromagnetic field from an intense pump laser pulse leads to replicas of the bands in energy, known as Floquet states. Floquet–Bloch states are then a result of periodic potentials in both time and in space. Floquet–Bloch states were demonstrated on the surface of a  $\text{Bi}_2\text{Se}_3$  sample by using a *p*-polarized pump pulse (FIG. 6e) with an energy lower than that of the bulk bandgap to avoid the excitations of abundant electron–hole pairs in the bulk, which can mask the observation<sup>64,182</sup>. Without pumping, a single Dirac-cone surface state resides inside the bulk bandgap (FIG. 6f). When pumping  $\text{Bi}_2\text{Se}_3$  with *p*-polarized laser pulses, periodic duplicates of the Dirac bands begin to appear along the energy axis (FIG. 6g,h), separated by the pump photon energy. These dispersive band replicas cross upon moving away from the  $\bar{\Gamma}$  point, giving rise to new crossing points (FIG. 6i). Notably, an energy gap of  $2\Delta$  opens along the  $k_y$  direction at the expected crossings while these crossings remain gapless along the  $k_x$  direction (FIG. 6g–i). This distinction between the two momentum directions is because the perturbing Hamiltonian associated with a *p*-polarized pulse commutes with the Dirac Hamiltonian for electrons with momentum along  $k_x$ , but not for those along  $k_y$  (REFS<sup>182,183</sup>). This gap opening along the  $k_y$  direction distinguishes the observed band replicas from those caused by laser-assisted photoemission, for which no gaps are expected<sup>64</sup>. The above observations provide direct evidence of the photon-dressed Floquet–Bloch states in solids and may pave the way for optical manipulation of new phases.

The capability of time-resolved ARPES goes far beyond the above two examples, and it has been widely used in studying the momentum-resolved electronic dynamics of many classes of materials, including high- $T_c$  superconductors (for example, cuprates<sup>63,65,184–192</sup> and iron-based superconductors<sup>66,193–197</sup>), density wave systems<sup>60–62,68,170,198,199</sup>, topological insulators<sup>64,67,182,200–207</sup>, graphene<sup>208–211</sup> and other strongly correlated systems<sup>212,213</sup>. For example, in addition to Floquet–Bloch states, the difference in dynamics of scattering between surface and bulk states has also been observed in  $\text{Bi}_2(\text{Se},\text{Te})_3$  (REFS<sup>200,201,207</sup>). Apart from incoherent transient

dynamics, coherently excited bosonic modes have also been observed in numerous materials, such as transition metal dichalcogenides<sup>60,170</sup>, rare-Earth tritellurides<sup>61,68,199</sup> and  $\text{FeSe}/\text{SrTiO}_3$  films<sup>197</sup>, often yielding important information about the electron–boson coupling in these systems.

### Spatially resolved ARPES

Typical synchrotron-based ARPES systems have a spatial resolution of  $\sim 100\ \mu\text{m}$ , depending on the spot size of the light source; thus, samples to be measured should have a flat surface with dimensions greater than  $100\ \mu\text{m}$ . However, many interesting materials or single-crystalline domains are smaller than  $100\ \mu\text{m}$ , such as heterostructures and microscale and nanoscale materials. In consideration of the above cases, spatially resolved ARPES with micrometre or sub-micrometre spatial resolution has been developed at several synchrotron light sources<sup>14,48–51,214</sup>.

Spatially resolved ARPES can be viewed as a combination of ARPES and scanning photoemission microscopy. Depending on the beam spot size, spatially resolved ARPES is referred to as micro-ARPES or nano-ARPES for microscale or nanoscale beams, respectively. To focus X-rays to a microscaled or nanosized spot at the sample, advanced optics have been developed, including Schwarzschild optics<sup>48</sup> and the Fresnel zone plate<sup>214</sup>. As an example, the nano-ARPES end-station<sup>50</sup> at the MAESTRO beamline at the Advanced Light Source (California, USA) uses a Fresnel zone plate to focus the beam, followed by an order-sorting aperture to eliminate high-diffraction orders (FIG. 7a). In general, a high-precision sample stage is also needed to ensure precise nanometre scanning and positioning of the sample. The final spatial resolution is determined by the resolution of the X-ray optics and the mechanical and thermal stability of the sample stage.

The development of spatially resolved ARPES has made it possible to map out the band structures of materials with high spatial resolution while maintaining the advantages of ARPES, such as good energy and momentum resolution. However, the shortcomings of spatially resolved ARPES include low count rates owing to the low focusing efficiency ( $\sim 1\%$ ) of the focusing optics, strong space-charge effects due to the nanosized beam spots, and limited photon-energy choices owing to the complexity of designing photon-energy-dependent focusing optics. A complementary technique, photoemission electron microscopy<sup>215</sup>, also enables spatially resolved electronic structure measurements. However, the corresponding energy and angular resolution (typically  $>100\ \text{meV}$  and  $1^\circ$ , respectively) of this technique are usually worse than those of spatially resolved ARPES (which has an energy resolution of the order of tens of meV and an angular resolution of  $\sim 0.1^\circ$ ).

### Application to weak topological insulators

Spatially resolved ARPES has been applied to the study of electronic structure of microscale and nanoscale materials and domains, including heterostructures<sup>52,53,216–223</sup>,  $\text{Sb}_2\text{Te}_3$  nanowires<sup>224,225</sup> and the weak topological insulator  $\beta\text{-Bi}_4\text{I}_4$  (REF.<sup>54</sup>). We highlight the

#### Photoemission electron microscopy

A surface-sensitive technique that uses photoemitted electrons from the surface; these electrons are accelerated and collected by an area detector to generate a magnified image of the surface.

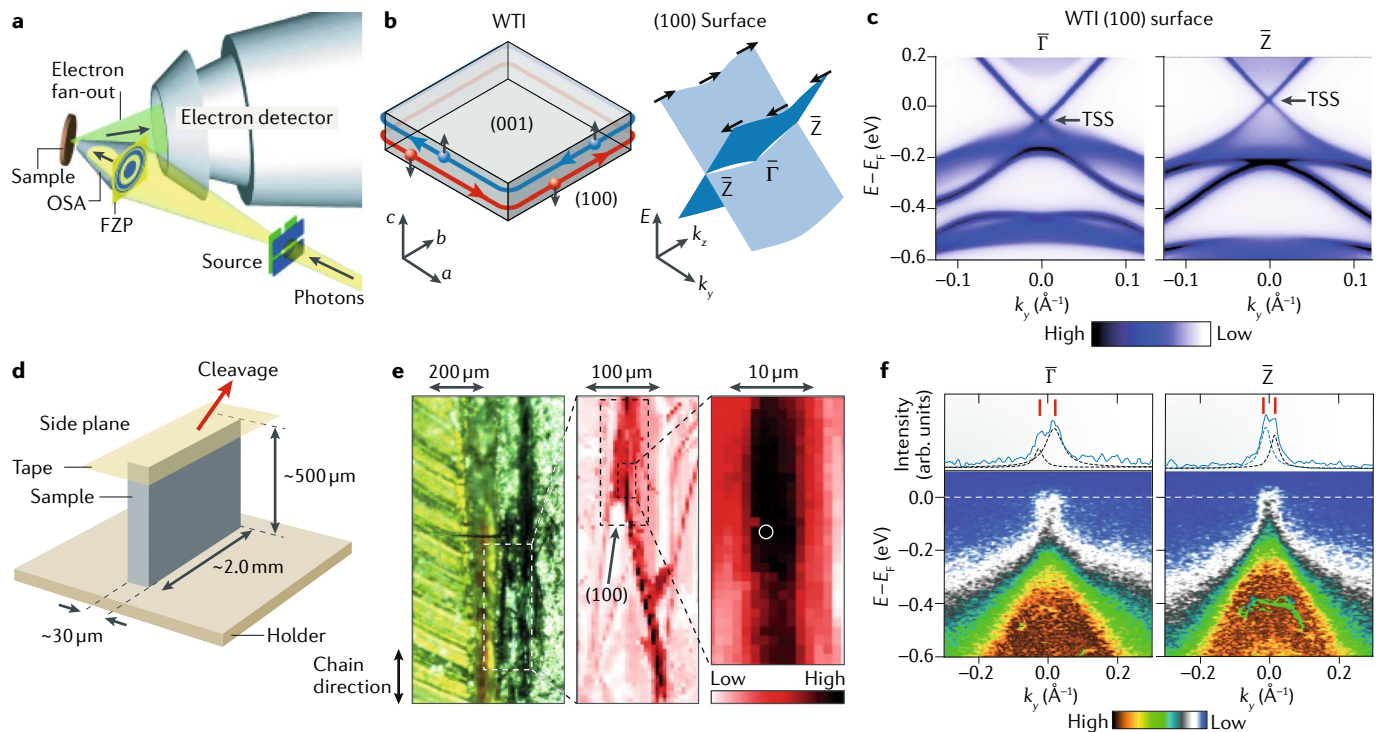


**Fig. 7 | Spatially resolved ARPES in the study of the topological surface states of  $\beta\text{-Bi}_4\text{I}_4$ .** Spatially resolved angle-resolved photoemission spectroscopy (ARPES) is a tool for studying the electronic structure of nanoscale or microscale materials and domains, such as the topological surface states of the weak topological insulator (WTI)  $\beta\text{-Bi}_4\text{I}_4$ . **a** | Schematic of a nano-ARPES system. A set of Fresnel zone plates (FZPs) is used to focus the incoming beam, followed by an order-sorting aperture (OSA) to suppress unwanted diffraction orders. **b** | Schematics of the topological surface states (TSSs) of  $\beta\text{-Bi}_4\text{I}_4$  in real space (left) and their band dispersions in  $\mathbf{k}$ -space (right), where  $k_y$  and  $k_x$  are the momenta in the  $y$  and  $x$  directions, respectively. The small spheres in the left part represent the electrons, with the black arrows indicating the spin texture of the electrons in real space; the blue and red arrows indicate the direction of electron movement. The black arrows in the right part indicate the spin texture in  $\mathbf{k}$ -space. **c** | Calculated Dirac band dispersions of TSSs at the  $\bar{\Gamma}$  (left) and  $\bar{Z}$  (right) points of the side (100) surface. **d** | Schematic showing the preparation of the (100) side surface for nano-ARPES measurements. Fresh side (100) surfaces can be obtained by cleaving  $\beta\text{-Bi}_4\text{I}_4$  samples using tape. **e** | The left part shows a real-space image of the measured  $\beta\text{-Bi}_4\text{I}_4$  sample taken using an optical microscope. The middle part shows a photoemission intensity map of the same  $\beta\text{-Bi}_4\text{I}_4$  sample, and the right part an enlargement of an area of this image. The white circle (with a diameter  $<1\ \mu\text{m}$ ) indicates the selected position for nano-ARPES measurements. **f** | ARPES intensity plots (bottom), and the momentum distribution curves (blue curves, top) at the Fermi level ( $E_F$ ) along the  $k_y$  direction at the  $\bar{\Gamma}$  (left) and  $\bar{Z}$  (right) points of the side (100) surface. The black dotted curves are the Lorentzian fitting of the two peak structures (indicated by red bars) in the momentum distribution curves.  $E$ , energy. Panel **a** is adapted with permission from REF.<sup>50</sup>, International Union of Crystallography. Panels **b–f** are adapted from REF.<sup>54</sup>, Springer Nature Limited.

recent application of spatially resolved ARPES in the study of  $\beta\text{-Bi}_4\text{I}_4$ , the first experimentally verified weak topological insulator.

In 3D, a topological insulator can be classified as either strong or weak depending on the  $Z_2$  topological invariants<sup>226,227</sup>. A strong topological insulator state, which manifests as gapless topological surface states at all the surfaces, has been experimentally confirmed in many materials, such as  $\text{Bi}_{1-x}\text{Sb}_x$  (REF.<sup>72</sup>) and  $\text{Bi}_2(\text{Se},\text{Te})_3$  (REFS<sup>43,44,73–75</sup>). By contrast, the weak topological insulator state is very challenging to detect, because the corresponding gapless surface states emerge only on particular surfaces, which are undetectable in most 3D crystals. Recently, using nano-ARPES, direct experimental evidence was obtained for the existence of a weak topological insulator state in  $\beta\text{-Bi}_4\text{I}_4$  through the observation of the topological Dirac surface states on the side (100)

surface<sup>54</sup> (FIG. 7b).  $\beta\text{-Bi}_4\text{I}_4$  exhibits no topological surface states on the (001) surface but exhibits quasi-1D topological surface states on the side (100) surface (FIG. 7b). These topological surface states exhibit two Dirac cones at the  $\bar{\Gamma}$  and  $\bar{Z}$  points (FIG. 7c), which, in principle, can be directly detected by ARPES. However,  $\beta\text{-Bi}_4\text{I}_4$  single crystals are typically very small ( $\sim 30\ \mu\text{m}$ ) along the stacking direction ( $c$  axis; FIG. 7d), and the cleaved (100) surface is composed of several small domains or stages (typically  $\sim 2\ \mu\text{m}$  in size). Therefore, it is difficult to study the surface states on the (100) surface by conventional ARPES, as the spot size ( $\sim 100\ \mu\text{m}$ ) of the incident beam is much larger than  $2\ \mu\text{m}$ . To selectively examine the Dirac surface states, a spatially resolved ARPES measurement with a beam spot  $<1\ \mu\text{m}$  was performed on the brightest region of the (100) surface (indicated by the white circle in the right part of FIG. 7e). This approach

made it possible to resolve the gapless Dirac dispersions expected at the  $\bar{\Gamma}$  and  $\bar{Z}$  points (FIG. 7f), hence demonstrating the experimental realization of the weak topological insulator state in  $\beta$ -Bi<sub>4</sub>I<sub>4</sub>.

### Conclusion

With the unique capability to directly visualize and discriminate surface and bulk electronic states, modern ARPES has had a central role in the study of topological materials.

Efforts over the past 30 years have dramatically improved the capabilities of ARPES. Achievements include the introduction of new cryostats, such as <sup>3</sup>He cryostats<sup>13</sup>, to enable the study of materials (such as low- $T_c$  superconductors) at sample temperatures <1 K. Moreover, the development of new types of electron analysers, such as DA30-L and ARTOF analysers, has increased performance and data acquisition efficiency, enabling the detection of 2D in-plane electronic structure at a fixed sample geometry. In terms of light sources, many advanced synchrotron-based VUV and soft-X-ray beamlines are now available, including the Dreamline at the Shanghai Synchrotron Radiation Facility (China), which has a high energy resolution (~25 meV at 1 keV) and a wide photon energy range (20–2,000 eV), and the I05 beamline<sup>18</sup> at Diamond (UK) and beamline 7.0.2 (REF.<sup>50</sup>) of the Advanced Light Source at the Lawrence Berkeley National Laboratory (USA), both of which have nanoscale beam spot sizes. The past 10 years has also witnessed the emergence of a new light source: X-ray free-electron lasers (XFELs)<sup>228–234</sup>. XFELs may be a promising light source for time-resolved ARPES owing to their tunable light spectrum and femtosecond-pulsed beams with a high photon flux. In particular, the wide tunability in energy makes it possible to perform systematic time-resolved ARPES measurements over the full 3D Brillouin zone, which is crucial for investigating the ultrafast dynamics of the bulk electronic structure of 3D materials such as topological semimetals. Nevertheless, the low repetition rate (usually tens to hundreds of hertz) of most XFELs is a major restriction for the application of time-resolved ARPES, because the pulse intensities must also be kept low to minimize space-charge effects. Therefore, the photoelectron count is not yet sufficient for acquiring time-resolved spectra within a reasonable time frame. However, the recently developed European XFEL (Germany) has a high repetition rate (up to 27 kHz)<sup>235</sup>, and the upgrade to the existing free-electron-laser source at the Linac Coherent Light Source (LCLS-II, USA) to achieve a repetition rate of 1 MHz is expected to commission in 2020. These developments thus provide a promising platform for performing next-generation time-resolved ARPES measurements with high-repetition-rate X-ray photons.

Looking forward, there remains substantial scope to improve the capabilities of ARPES. High-momentum and energy-resolution laser ARPES with <sup>3</sup>He cryostats is needed to probe the superconducting gap of low- $T_c$  superconductors; this technique is already under development in several laboratories. Despite great interest, spin-resolved soft-X-ray ARPES has still not been realized, owing to the poor efficiency of the spin detectors

and the low cross sections of soft-X-ray photoemission. The development of high-efficiency spin detectors and ultrabright synchrotron light will make it possible to perform spin-resolved ARPES measurements in the soft-X-ray regime. Indeed, scientists at several advanced soft-X-ray beamlines, such as the Advanced Resonant Spectroscopies beamline at the Swiss Light Source and the Dreamline at the Shanghai Synchrotron Radiation Facility, have already started working on adding high-efficiency spin spectrometers to their ARPES systems<sup>160</sup>. With continued improvements in the focusing optics, we also expect that the efficiency of spatially resolved ARPES will improve. For time-resolved ARPES, it remains necessary to develop high-repetition-rate and stable laboratory-based lasers with tunable probe photon energy and high photon flux. At the same time, the development of strong tunable pump pulses from the ultraviolet down to the terahertz range is essential for the study of coherent and/or resonant excitations of low-energy modes, such as lattice vibrations, and various quasiparticle excitations in non-trivial band structures. Indeed, the first time-resolved ARPES system with a terahertz pump laser was reported in 2018 (REF.<sup>67</sup>) and successfully applied to the study of Dirac fermions in Bi<sub>2</sub>Te<sub>3</sub>. Furthermore, the combination of high-efficiency spin detectors with time-resolved ARPES systems would provide new opportunities for simultaneously acquiring time-resolved and spin-resolved ARPES spectra. For example, a high-efficiency ARTOF–VLEED spin spectrometer that combines a VLEED spin detector with an ARTOF analyser has been developed<sup>155,236</sup>. This high-efficiency spectrometer enables simultaneous spin-resolved, time-resolved and angle-resolved photoemission with pulsed lasers<sup>237</sup>. Lastly, combining ARPES with advanced methods of sample synthesis (for example, molecular beam epitaxy and pulsed laser deposition) and other complementary in situ characterization techniques (such as a scanning tunnelling microscopy, optical spectroscopy and transport measurements) would provide an efficient platform to systematically design and synthesize new materials, as well as to investigate their physical properties.

Although ARPES has facilitated the discovery and understanding of the unique physical properties of many topological materials, including topological insulators, topological Dirac and Weyl semimetals and unconventional fermions, there are still several prominent physics problems waiting to be explored using this technique. For example, the spin texture of bulk Weyl cones has not yet been investigated owing to the lack of spin-resolved soft-X-ray ARPES systems. Moreover, many predicted topological phases, such as magnetic Weyl semimetals<sup>88,89</sup>, still await strong electronic-structure evidence from ARPES to establish their existence. The recent discovery of superconductivity in twisted bilayer graphene<sup>238,239</sup> has attracted extensive attention, and the interesting electronic structure might be resolved by spatially resolved ARPES. Hence, we strongly believe that ARPES will continue to have a leading role in the research into topological materials in the future.

Published online: 27 August 2019

1. Bednorz, J. G. & Müller, K. A. Possible high  $T_c$  superconductivity in the Ba–La–Cu–O System. *Z. Phys. B* **64**, 267–271 (1986).
2. Kamihara, Y., Watanabe, T., Hirano, M. & Hosono, H. Iron-based layered superconductor  $\text{LaO}_{1-x}\text{F}_x\text{FeAs}$  ( $x = 0.05\text{--}0.12$ ) with  $T_c = 26$  K. *J. Am. Chem. Soc.* **130**, 3296–3297 (2008).
3. Hall, E. H. On a new action of the magnet on electric currents. *Am. J. Math.* **2**, 287–292 (1879).
4. Klitzing, K. V., Dorda, G. & Pepper, M. New method for high-accuracy determination of the fine-structure constant based on quantized Hall resistance. *Phys. Rev. Lett.* **45**, 494–497 (1980).
5. Tsui, D. C., Stormer, H. L. & Gossard, A. C. Two-dimensional magnetotransport in the extreme quantum limit. *Phys. Rev. Lett.* **48**, 1559–1562 (1982).
6. König, M. et al. Quantum spin Hall insulator state in HgTe quantum wells. *Science* **318**, 766–770 (2007).
7. Chang, C.-Z. et al. Experimental observation of the quantum anomalous Hall effect in a magnetic topological insulator. *Science* **340**, 167–170 (2013).
8. Damaschelli, A., Hussain, Z. & Shen, Z.-X. Angle-resolved photoemission studies of the cuprate superconductors. *Rev. Mod. Phys.* **75**, 473 (2003).
9. Hüfner, S. *Photoelectron Spectroscopy: Principles and Applications* (Springer, 2003).  
**A classic textbook on photoemission spectroscopy.**
10. Campuzano, J. C., Norman, M. R. & Randeria, M. *Photoemission in the High  $T_c$  Superconductors. The Physics of Superconductors 167–273* (Springer, 2004).
11. Kirchmann, P. S. et al. A time-of-flight spectrometer for angle-resolved detection of low energy electrons in two dimensions. *Appl. Phys. A* **91**, 211–217 (2008).
12. Saitoh, Y. et al. Performance of a very high resolution soft X-ray beamline BL25SU with a twin-helical undulator at SPring-8. *Rev. Sci. Instrum.* **71**, 3254–3259 (2000).
13. Borisenko, S. V. ‘One-cubed’ ARPES User Facility at BESSY II. *Synchrotron Radiat. News* **25**, 6–11 (2012).
14. Reininger, R. et al. The electron spectro-microscopy beamline at National Synchrotron Light Source II: A wide photon energy range, micro-focusing beamline for photoelectron spectro-microscopies. *Rev. Sci. Instrum.* **83**, 23102 (2012).
15. Tamura, L. et al. Advanced light source update. *Synchrotron Radiat. News* **25**, 25–30 (2012).
16. Strocov, V. N. et al. Soft-X-ray ARPES facility at the ADRESS beamline of the SLS: concepts, technical realisation and scientific applications. *J. Synchrotron Radiat.* **21**, 32–44 (2014).
17. Cerenius, Y., Hennies, F. & Fernandes Tavares, P. Status of the MAX IV Laboratory. *Synchrotron Radiat. News* **29**, 34–38 (2016).
18. Hoesch, M. et al. A facility for the analysis of the electronic structures of solids and their surfaces by synchrotron radiation photoelectron spectroscopy. *Rev. Sci. Instrum.* **88**, 13106 (2017).
19. Koralek, J. D. et al. Experimental setup for low-energy laser-based angle resolved photoemission spectroscopy. *Rev. Sci. Instrum.* **78**, 53905 (2007).
20. Mathias, S. et al. Angle-resolved photoemission spectroscopy with a femtosecond high harmonic light source using a two-dimensional imaging electron analyzer. *Rev. Sci. Instrum.* **78**, 83105 (2007).
21. Liu, G. et al. Development of a vacuum ultraviolet laser-based angle-resolved photoemission system with a superhigh energy resolution better than 1 meV. *Rev. Sci. Instrum.* **79**, 23105 (2008).
22. Kiss, T. et al. A versatile system for ultrahigh resolution, low temperature, and polarization dependent Laser-angle-resolved photoemission spectroscopy. *Rev. Sci. Instrum.* **79**, 23106 (2008).
23. He, Y. et al. Invited article: high resolution angle resolved photoemission with tabletop 11 eV laser. *Rev. Sci. Instrum.* **87**, 11301 (2016).
24. Peng, Q.-J. et al. DUV/VUV All-solid-state lasers: twenty years of progress and the future. *IEEE J. Sel. Top. Quantum Electron.* **24**, 1–12 (2018).
25. Zhou, X. et al. New developments in laser-based photoemission spectroscopy and its scientific applications: a key issues review. *Rep. Prog. Phys.* **81**, 62101 (2018).
26. Okazaki, K. et al. Octet-line node structure parameter in  $\text{KFe}_2\text{As}_2$ . *Science* **337**, 1314–1317 (2012).
27. Zhang, W. et al. High energy dispersion relations for the high temperature  $\text{Bi}_2\text{Sr}_2\text{CaCu}_2\text{O}_8$  superconductor from laser-based angle-resolved photoemission spectroscopy. *Phys. Rev. Lett.* **101**, 17002 (2008).
28. Bok, J. M. et al. Quantitative determination of pairing interactions for high-temperature superconductivity in cuprates. *Sci. Adv.* **2**, e1501329 (2016).
29. Lee, J. J. et al. Interfacial mode coupling as the origin of the enhancement of  $T_c$  in FeSe films on  $\text{SrTiO}_3$ . *Nature* **515**, 245–248 (2014).
30. Strocov, V. N. et al. Three-dimensional electron realm in VSe<sub>2</sub> by soft-X-ray photoelectron spectroscopy: origin of charge-density waves. *Phys. Rev. Lett.* **109**, 86401 (2012).
31. Lev, L. L. et al. Fermi surface of three-dimensional  $\text{La}_{1-x}\text{Sr}_x\text{MnO}_3$  explored by soft-X-ray ARPES: rhombohedral lattice distortion and its effect on magnetoresistance. *Phys. Rev. Lett.* **114**, 237601 (2015).
32. Fadley, C. S. Looking deeper: angle-resolved photoemission with soft and hard X-rays. *Synchrotron Radiat. News* **25**, 26–31 (2012).
33. Lv, B. Q. et al. Observation of Weyl nodes in TaAs. *Nat. Phys.* **11**, 724–727 (2015).
34. Xu, S.-Y. et al. Discovery of a Weyl fermion semimetal and topological Fermi arcs. *Science* **349**, 613–617 (2015).  
**A pioneering ARPES study reporting the experimental discovery of Weyl fermions in condensed matter systems.**
35. Lv, B. Q. et al. Observation of three-component fermions in the topological semimetal molybdenum phosphide. *Nature* **546**, 627–631 (2017).  
**The initial report of the observation of unconventional three-component fermions in solids using soft-X-ray ARPES.**
36. Ma, J.-Z. et al. Three-component fermions with surface Fermi arcs in tungsten carbide. *Nat. Phys.* **14**, 349–354 (2018).
37. Yang, L. X. et al. Weyl semimetal phase in the non-centrosymmetric compound TaAs. *Nat. Phys.* **11**, 728–732 (2015).
38. Hoesch, M. et al. Spin-polarized Fermi surface mapping. *J. Electron Spectrosc. Relat. Phenom.* **124**, 263–279 (2002).
39. Dil, J. H. Spin and angle resolved photoemission on non-magnetic low-dimensional systems. *J. Phys. Condens. Matter* **21**, 403001 (2009).
40. Yaji, K. et al. High-resolution three-dimensional spin- and angle-resolved photoelectron spectrometer using vacuum ultraviolet laser light. *Rev. Sci. Instrum.* **87**, 53111 (2016).
41. Okuda, T. Recent trends in spin-resolved photoelectron spectroscopy. *J. Phys. Condens. Matter* **29**, 483001 (2017).
42. Ji, F. et al. Multichannel exchange-scattering spin polarimetry. *Phys. Rev. Lett.* **116**, 177601 (2016).
43. Hsieh, D. et al. A tunable topological insulator in the spin helical Dirac transport regime. *Nature* **460**, 1101–1105 (2009).  
**A spin-resolved ARPES study that provides direct experimental evidence that topological insulators possess a spin-momentum locking feature.**
44. Hsieh, D. et al. Observation of unconventional quantum spin textures in topological insulators. *Science* **323**, 919–922 (2009).
45. Lv, B. Q. et al. Observation of Fermi-arc spin texture in TaAs. *Phys. Rev. Lett.* **115**, 217601 (2015).
46. Xu, N., Ding, H. & Shi, M. Spin- and angle-resolved photoemission on the topological Kondo insulator candidate:  $\text{SmB}_6$ . *J. Phys. Condens. Matter* **28**, 363001 (2016).
47. Plumb, N. C. & Radović, M. Angle-resolved photoemission spectroscopy studies of metallic surface and interface states of oxide insulators. *J. Phys. Condens. Matter* **29**, 433005 (2017).
48. Dudin, P. et al. Angle-resolved photoemission spectroscopy and imaging with a submicrometre probe at the SPECTROMICROSCOPY-3.2L beamline of Elettra. *J. Synchrotron Radiat.* **17**, 445–450 (2010).
49. Avila, J. & Asensio, M. C. First nanoARPES user facility available at SOLEIL: an innovative and powerful tool for studying advanced materials. *Synchrotron Radiat. News* **27**, 24–30 (2014).
50. Rotenberg, E. & Bostwick, A. MicroARPES and nanoARPES at diffraction-limited light sources: opportunities and performance gains. *J. Synchrotron Radiat.* **21**, 1048–1056 (2014).
51. Koch, R. J. et al. Nano focusing of soft X-rays by a new capillary mirror optic. *Synchrotron Radiat. News* **31**, 50–52 (2018).
52. Avila, J. et al. Exploring electronic structure of one-atom thick polycrystalline graphene films: a nano angle resolved photoemission study. *Sci. Rep.* **3**, 2439 (2013).
53. Singh, S. et al. Giant spin-splitting and gap renormalization driven by trions in single-layer  $\text{WS}_2/\text{h-BN}$  heterostructures. *Nat. Phys.* **14**, 355–359 (2018).
54. Noguchi, R. et al. A weak topological insulator state in quasi-one-dimensional bismuth iodide. *Nature* **566**, 518–522 (2019).
55. Ishida, Y. et al. High repetition pump-and-probe photoemission spectroscopy based on a compact fiber laser system. *Rev. Sci. Instrum.* **87**, 123902 (2016).
56. Smallwood, C. L., Kaindl, R. A. & Lanzara, A. Ultrafast angle-resolved photoemission spectroscopy of quantum materials. *EPL* **115**, 27001 (2016).
57. Rohde, G. et al. Time-resolved ARPES with sub-15 fs temporal and near Fourier-limited spectral resolution. *Rev. Sci. Instrum.* **87**, 103102 (2016).
58. Cavalieri, A. L. et al. Attosecond spectroscopy in condensed matter. *Nature* **449**, 1029–1032 (2007).
59. Tao, Z., Keller, M., Mavrikakis, M., Kapteyn, H. & Murnane, M. Direct time-domain observation of attosecond final-state lifetimes in photoemission from solids. *Science* **353**, 62–67 (2016).
60. Perfetti, L. et al. Time evolution of the electronic structure of 1T-TaS<sub>2</sub> through the insulator–metal transition. *Phys. Rev. Lett.* **97**, 67402 (2006).
61. Schmitt, F. et al. Transient electronic structure and melting of a charge density wave in  $\text{TbTe}_3$ . *Science* **321**, 1649–1652 (2008).
62. Rohwer, T. et al. Collapse of long-range charge order tracked by time-resolved photoemission at high momenta. *Nature* **471**, 490–493 (2011).
63. Smallwood, C. L. et al. Tracking Cooper pairs in a cuprate superconductor by ultrafast angle-resolved photoemission. *Science* **336**, 1137–1139 (2012).
64. Wang, Y. H., Steinberg, H., Jarillo-Herrero, P. & Gedik, N. Observation of Floquet–Bloch states on the surface of a topological insulator. *Science* **342**, 453–457 (2013).  
**A time-resolved ARPES study reporting the observation of Floquet–Bloch states on the surface of  $\text{Bi}_2\text{Se}_3$ .**
65. Greven, M., Damaschelli, A., Avella, A. & Fausti, D. Signatures of enhanced superconducting phase coherence in optimally doped  $\text{Bi}_{25}\text{F}_2\text{Y}_{0.08}\text{Ca}_{0.92}\text{Cu}_2\text{O}_{8+\delta}$  driven by midinfrared pulse excitations. *Phys. Rev. Lett.* **122**, 67002 (2019).
66. Rettig, L. et al. Ultrafast momentum-dependent response of electrons in antiferromagnetic  $\text{EuFe}_2\text{As}_2$  driven by optical excitation. *Phys. Rev. Lett.* **108**, 97002 (2012).
67. Reimann, J. et al. Subcycle observation of lightwave-driven Dirac currents in a topological surface band. *Nature* **562**, 396–400 (2018).
68. Zong, A. et al. Evidence for topological defects in a photoinduced phase transition. *Nat. Phys.* **15**, 27–31 (2019).
69. Belopolski, I. et al. Discovery of a new type of topological Weyl fermion semimetal state in  $\text{Mo}_x\text{W}_{1-x}\text{Te}_2$ . *Nat. Commun.* **7**, 13643 (2016).
70. Zhang, P. et al. Topologically entangled Rashba–split Shockley states on the surface of grey arsenic. *Phys. Rev. Lett.* **118**, 46802 (2017).
71. Belopolski, I. et al. Signatures of a time-reversal symmetric Weyl semimetal with only four Weyl points. *Nat. Commun.* **8**, 942 (2017).
72. Hsieh, D. et al. A topological Dirac insulator in a quantum spin Hall phase. *Nature* **452**, 970–974 (2008).  
**Study reporting the experimental realization of a 3D topological insulator,  $\text{Bi}_2\text{Sb}_3$ .**
73. Zhang, H. et al. Topological insulators in  $\text{Bi}_2\text{Se}_3$ ,  $\text{Bi}_2\text{Te}_3$  and  $\text{Sb}_2\text{Te}_3$  with a single Dirac cone on the surface. *Nat. Phys.* **5**, 438–442 (2009).
74. Xia, Y. et al. Observation of a large-gap topological-insulator class with a single Dirac cone on the surface. *Nat. Phys.* **5**, 398–402 (2009).  
**Study reporting the experimental realization of an excellent 3D topological insulator,  $\text{Bi}_2\text{Se}_3$ , with a large bulk bandgap and a single surface Dirac cone.**
75. Chen, Y. L. et al. Experimental realization of a three-dimensional topological insulator,  $\text{Bi}_2\text{Te}_3$ . *Science* **325**, 178–181 (2009).
76. Hasan, M. Z. & Kane, C. L. Colloquium: topological insulators. *Rev. Mod. Phys.* **82**, 3045–3067 (2010).
77. Qi, X. L. & Zhang, S. C. Topological insulators and superconductors. *Rev. Mod. Phys.* **83**, 1057 (2011).
78. Fu, L. Topological crystalline insulators. *Phys. Rev. Lett.* **106**, 106802 (2011).
79. Hsieh, T. H. et al. Topological crystalline insulators in the  $\text{SnTe}$  material class. *Nat. Commun.* **3**, 982 (2012).
80. Tanaka, Y. et al. Experimental realization of a topological crystalline insulator in  $\text{SnTe}$ . *Nat. Phys.* **8**, 800–803 (2012).
81. Wang, Z., Alexandradinata, A., Cava, R. J. & Bernevig, B. A. Hourglass fermions. *Nature* **532**, 189–194 (2016).
82. Ma, J. et al. Experimental evidence of hourglass fermion in the candidate nonsymmorphic topological insulator  $\text{KHgSb}$ . *Sci. Adv.* **3**, e1602415 (2017).

83. Young, S. M. et al. Dirac semimetal in three dimensions. *Phys. Rev. Lett.* **108**, 140405 (2012).
84. Wang, Z. et al. Dirac semimetal and topological phase transitions in  $A_2Bi$  ( $A=Na, K, Rb$ ). *Phys. Rev. B* **85**, 195320 (2012).
85. Wang, Z., Weng, H., Wu, Q., Dai, X. & Fang, Z. Three-dimensional Dirac semimetal and quantum transport in  $Cd_3As_2$ . *Phys. Rev. B* **88**, 125427 (2013).
86. Liu, Z. K. et al. A stable three-dimensional topological Dirac semimetal  $Cd_3As_2$ . *Nat. Mater.* **13**, 677–681 (2014).
87. Liu, Z. K. et al. Discovery of a three-dimensional topological dirac semimetal,  $Na_3Bi$ . *Science* **343**, 864–867 (2014).
- Experimental study reporting the discovery of 3D massless Dirac fermions in a topological Dirac semimetal.**
88. Wan, X., Turner, A. M., Vishwanath, A. & Savrasov, S. Y. Topological semimetal and Fermi-arc surface states in the electronic structure of pyrochlore iridates. *Phys. Rev. B* **83**, 205101 (2011).
89. Xu, G., Weng, H., Wang, Z., Dai, X. & Fang, Z. Chern semimetal and the quantized anomalous Hall effect in  $HgCr_2Se_4$ . *Phys. Rev. Lett.* **107**, 186806 (2011).
90. Huang, S. M. et al. A Weyl fermion semimetal with surface Fermi arcs in the transition metal mononitride TaAs class. *Nat. Commun.* **6**, 7373 (2015).
91. Lv, B. Q. et al. Experimental discovery of Weyl semimetal TaAs. *Phys. Rev. X* **5**, 31013 (2015).
- A pioneering experimental ARPES study that reports the discovery of Weyl fermions in condensed matter systems.**
92. Soluyanov, A. A. et al. Type-II Weyl semimetals. *Nature* **527**, 495–498 (2015).
93. Huang, L. et al. Spectroscopic evidence for a type II Weyl semimetallic state in  $MoTe_2$ . *Nat. Mater.* **15**, 1155–1160 (2016).
94. Deng, K. et al. Experimental observation of topological Fermi arcs in type-II Weyl semimetal  $MoTe_2$ . *Nat. Phys.* **12**, 1105–1110 (2016).
95. Weng, H., Fang, C., Fang, Z., Bernevig, A. & Dai, X. Weyl semimetal phase in noncentrosymmetric transition-metal monophosphides. *Phys. Rev. X* **5**, 11029 (2015).
96. Richard, P., Sato, T., Nakayama, K., Takahashi, T. & Ding, H. Fe-based superconductors: an angle-resolved photoemission spectroscopy perspective. *Rep. Prog. Phys.* **74**, 124512 (2011).
97. Richard, P., Qian, T. & Ding, H. ARPES measurements of the superconducting gap of Fe-based superconductors and their implications to the pairing mechanism. *J. Phys. Condens. Matter* **27**, 293203 (2015).
98. Lu, D. et al. Angle-resolved photoemission studies of quantum materials. *Annu. Rev. Condens. Matter Phys.* **3**, 129–167 (2012).
99. Ye, Z.-R., Zhang, Y., Xie, B.-P. & Feng, D.-L. Angle-resolved photoemission spectroscopy study on iron-based superconductors. *Chin. Phys. B* **22**, 87407 (2013).
100. Yang, H. et al. Visualizing electronic structures of quantum materials by angle-resolved photoemission spectroscopy. *Nat. Rev. Mater.* **3**, 341–353 (2018).
101. Hertz, H. Ueber einen Einfluss des ultravioletten Lichtes auf die elektrische Entladung. *Ann. Phys.* **17**, 983–1000 (1887).
102. Einstein, A. Über einen die Erzeugung und Verwandlung des Lichtes betreffenden heuristischen Gesichtspunkt. *Ann. Phys.* **322**, 132–148 (1905).
103. Ossianer, M. et al. Absolute timing of the photoelectric effect. *Nature* **561**, 374–377 (2018).
104. Xu, Y.-M. et al. Observation of a ubiquitous three-dimensional superconducting gap function in optimally doped  $Ba_{0.6}K_{0.4}Fe_2As_2$ . *Nat. Phys.* **7**, 198–202 (2011).
105. Zhang, Y. et al. Nodal superconducting-gap structure in ferropnictide superconductor  $BaFe_2(As_{0.7}P_{0.3})_2$ . *Nat. Phys.* **8**, 371–375 (2012).
106. Zhang, Y. et al. Symmetry breaking via orbital-dependent reconstruction of electronic structure in detwinned  $NaFeAs$ . *Phys. Rev. B* **85**, 85121 (2012).
107. Wang, X.-P. et al. Orbital characters determined from Fermi surface intensity patterns using angle-resolved photoemission spectroscopy. *Phys. Rev. B* **85**, 214518 (2012).
108. Vilmercati, P. et al. Evidence for three-dimensional Fermi-surface topology of the layered electron-doped iron superconductor  $Ba(Fe_{1-x}Co_x)_2As_2$ . *Phys. Rev. B* **79**, 220503 (2009).
109. Yi, M. et al. Symmetry-breaking orbital anisotropy observed for detwinned  $Ba(Fe_{1-x}Co_x)_2As_2$  above the spin density wave transition. *Proc. Natl Acad. Sci. USA* **108**, 6878–6883 (2011).
110. Seah, M. & Dench, W. Quantitative electron spectroscopy of surfaces. *Surf. Interface Anal.* **2**, 2–11 (1979).
111. He, S. et al. Phase diagram and electronic indication of high-temperature superconductivity at 65 K in single-layer FeSe films. *Nat. Mater.* **12**, 605–610 (2013).
112. Tan, S. et al. Interface-induced superconductivity and strain-dependent spin density waves in  $FeSe/SrTiO_3$  thin films. *Nat. Mater.* **12**, 634–640 (2013).
113. Shi, X. et al. Enhanced superconductivity accompanying a Lifshitz transition in electron-doped FeSe monolayer. *Nat. Commun.* **8**, 14988 (2017).
114. Wu, Y. et al. Electronic structure of the topological superconductor candidate  $Au_2Pb$ . *Phys. Rev. B* **98**, 161107 (2018).
115. Sanchez, D. S. et al. Topological chiral crystals with helicoid-arc quantum states. *Nature* **567**, 500–505 (2019).
116. Rao, Z. et al. Observation of unconventional chiral fermions with long Fermi arcs in  $CoSi$ . *Nature* **567**, 496–499 (2019).
117. Souma, S., Sato, T., Takahashi, T. & Baltzer, P. High-intensity xenon plasma discharge lamp for bulk-sensitive high-resolution photoemission spectroscopy. *Rev. Sci. Instrum.* **78**, 123104 (2007).
118. Annemie, Bogaerts, Neyts, E., Gijbels, R., Mullen, J. & Van der. Gas discharge plasmas and their applications. *Spectrochim. Acta B* **57**, 609–658 (2002).
119. Thompson, A. et al. *X-ray Data Booklet*. <http://cxro.lbl.gov/PDF/X-Ray-Data-Booklet.pdf> (LBNL Center for X-ray Optics, 2009).
120. Zhou, X. J. et al. Space charge effect and mirror charge effect in photoemission spectroscopy. *J. Electron Spectros. Relat. Phenom.* **142**, 27–38 (2005).
121. Passlack, S. et al. Space charge effects in photoemission with a low repetition, high intensity femtosecond laser source. *J. Appl. Phys.* **100**, 24912 (2006).
122. Hellmann, S., Rosnagel, K., Marczynski-Bühlow, M. & Kipp, L. Vacuum space-charge effects in solid-state photoemission. *Phys. Rev. B* **79**, 35402 (2009).
123. Fang, Z. et al. The anomalous Hall effect and magnetic monopoles in momentum space. *Science* **302**, 92–95 (2003).
124. Weyl, H. Electron and gravitation. *Z. Phys.* **56**, 330–352 (1929).
125. Dakovski, G. L., Li, Y., Durakiewicz, T. & Rodriguez, G. Tunable ultrafast extreme ultraviolet source for time- and angle-resolved photoemission spectroscopy. *Rev. Sci. Instrum.* **81**, 73108 (2010).
126. Berntsen, M. H., Götberg, O. & Tjernberg, O. An experimental setup for high resolution 10.5 eV laser-based angle-resolved photoelectron spectroscopy using a time-of-flight electron analyzer. *Rev. Sci. Instrum.* **82**, 95113 (2011).
127. Frietsch, B. et al. A high-order harmonic generation apparatus for time- and angle-resolved photoelectron spectroscopy. *Rev. Sci. Instrum.* **84**, 75106 (2013).
128. Winterfeldt, C., Spielmann, C. & Gerber, G. Colloquium: Optimal control of high-harmonic generation. *Rev. Mod. Phys.* **80**, 117–140 (2008).
129. Koch, T. L. & Bowers, J. E. Nature of wavelength chirping in directly modulated semiconductor lasers. *Electron. Lett.* **20**, 1038–1040 (1984).
130. Zhang, P. et al. Observation of topological superconductivity on the surface of an iron-based superconductor. *Science* **360**, 182–186 (2018).
- Study in which high-resolution laser-ARPES measurements provide direct evidence for the existence of topological superconductivity on the (001) surface of an iron-based superconductor.**
131. Hsu, F.-C. et al. Superconductivity in the PbO-type structure  $\alpha$ - $FeSe$ . *Proc. Natl. Acad. Sci. USA* **105**, 14262–14264 (2008).
132. Wang, Z. et al. Topological nature of the  $FeSe_{0.5}Te_{0.5}$  superconductor. *Phys. Rev. B* **92**, 115119 (2015).
133. Wu, X., Qin, S., Liang, Y., Fan, H. & Hu, J. Topological characters in  $Fe(Te_{1-x}Se_x)$  thin films. *Phys. Rev. B* **93**, 115129 (2016).
134. Xu, G., Lian, B., Tang, P., Qi, X. & Zhang, S. Topological superconductivity on the surface of Fe-based superconductors. *Phys. Rev. Lett.* **117**, 47001 (2016).
135. Chen, F. et al. Electronic structure of  $Fe_{1.04}Te_{0.66}Se_{0.34}$ . *Phys. Rev. B* **81**, 14526 (2010).
136. Miao, H. et al. Isotropic superconducting gaps with enhanced pairing on electron Fermi surfaces in  $FeTe_{0.55}Se_{0.45}$ . *Phys. Rev. B* **85**, 94506 (2012).
137. Fu, L. & Kane, C. L. Superconducting proximity effect and Majorana fermions at the surface of a topological insulator. *Phys. Rev. Lett.* **100**, 96407 (2008).
138. Wang, D. et al. Evidence for majorana bound states in an iron-based superconductor. *Science* **362**, 333–335 (2018).
139. Solterbeck, C. & Schattke, W. Energetic and spatial bonding properties from angular distributions of ultraviolet photoelectrons: application to the  $GaAs(110)$  surface. *Phys. Rev. Lett.* **79**, 4681 (1997).
140. Yeh, J. J. & Lindau, I. Atomic subshell photoionization cross sections and asymmetry parameters:  $1 \leq Z \leq 103$ . *Data Nucl. Data Tables* **32**, 1–155 (1985).
141. Heikkilä, T. T. & Volovik, G. E. Nexus and Dirac lines in topological materials. *New J. Phys.* **17**, 93019 (2015).
142. Wieder, B. J., Kim, Y., Rappe, A. M. & Kane, C. L. Double Dirac semimetals in three dimensions. *Phys. Rev. Lett.* **116**, 186402 (2016).
143. Bradlyn, B. et al. Beyond Dirac and Weyl fermions: unconventional quasiparticles in conventional crystals. *Science* **353**, aaf5037 (2016).
144. Weng, H., Fang, C., Fang, Z. & Dai, X. Coexistence of Weyl fermion and massless triply degenerate nodal points. *Phys. Rev. B* **94**, 165201 (2016).
145. Weng, H., Fang, C., Fang, Z. & Dai, X. Topological semimetals with triply degenerate nodal points in  $\theta$ -phase tantalum nitride. *Phys. Rev. B* **93**, 241202 (2016).
146. Zhu, Z., Winkler, G. W., Wu, Q., Li, J. & Soluyanov, A. A. Triple point topological metals. *Phys. Rev. X* **6**, 31003 (2016).
147. Chang, G. et al. Unconventional chiral fermions and large topological Fermi arcs in  $RhSi$ . *Phys. Rev. Lett.* **119**, 206401 (2017).
148. Tang, P., Zhou, Q. & Zhang, S.-C. Multiple types of topological fermions in transition metal silicides. *Phys. Rev. Lett.* **119**, 206402 (2017).
149. Zhang, T. et al. Double-Weyl phonons in transition-metal monosilicides. *Phys. Rev. Lett.* **120**, 016401 (2018).
150. Jia, S., Xu, S.-Y. & Hasan, M. Z. Weyl semimetals, Fermi arcs and chiral anomalies. *Nat. Mater.* **15**, 1140–1144 (2016).
151. Kirschner, J. & Feder, R. Spin polarization in double diffraction of low-energy electrons from  $W(001)$ : experiment and theory. *Phys. Rev. Lett.* **42**, 1008–1011 (1979).
152. Unguris, J., Pierce, D. T. & Celotta, R. J. Low-energy diffuse scattering electron-spin polarization analyzer. *Rev. Sci. Instrum.* **57**, 1314–1323 (1986).
153. Tillmann, D., Thiel, R. & Kisker, E. Very-low-energy spin-polarized electron diffraction from  $Fe(001)$ . *Z. Phys. B* **77**, 1–2 (1989).
154. Winkelmann, A., Hartung, D., Engelhard, H., Chiang, C.-T. & Kirschner, J. High efficiency electron spin polarization analyzer based on exchange scattering at  $FeW(001)$ . *Rev. Sci. Instrum.* **79**, 83303 (2008).
155. Jozwiak, C. et al. A high-efficiency spin-resolved photoemission spectrometer combining time-of-flight spectroscopy with exchange-scattering polarimetry. *Rev. Sci. Instrum.* **81**, 53904 (2010).
156. Souma, S., Takayama, A., Sugawara, K., Sato, T. & Takahashi, T. Ultrahigh-resolution spin-resolved photoemission spectrometer with a mini Mott detector. *Rev. Sci. Instrum.* **81**, 95101 (2010).
157. Berntsen, M. H. et al. A spin- and angle-resolving photoelectron spectrometer. *Rev. Sci. Instrum.* **81**, 35104 (2010).
158. Okuda, T. et al. Efficient spin resolved spectroscopy observation machine at Hiroshima Synchrotron Radiation Center. *Rev. Sci. Instrum.* **82**, 103302 (2011).
159. Kolbe, M. et al. Highly efficient multichannel spin-polarization detection. *Phys. Rev. Lett.* **107**, 207601 (2011).
160. Strocov, V. N., Petrov, V. N. & Dil, J. H. Concept of a multi-channel spin-resolving electron analyzer based on Mott scattering. *J. Synchrotron Radiat.* **22**, 708–716 (2015).
161. Jozwiak, C. et al. Widespread spin polarization effects in photoemission from topological insulators. *Phys. Rev. B* **84**, 165113 (2011).
162. Heinzmann, U. & Dil, J. H. Spin-orbit-induced photoelectron spin polarization in angle-resolved photoemission from both atomic and condensed matter targets. *J. Phys. Condens. Matter* **24**, 173001 (2012).
163. Osterwalder, J. Can spin-polarized photoemission measure spin properties in condensed matter? *J. Phys. Condens. Matter* **24**, 171001 (2012).
164. Westphal, C., Bansmann, J., Getzlaff, M. & Schönhense, G. Circular dichroism in the angular distribution of photoelectrons from oriented CO molecules. *Phys. Rev. Lett.* **63**, 151–154 (1989).
165. Schneider, C. M. & Kirschner, J. Spin- and angle-resolved photoelectron spectroscopy from solid surfaces with circularly polarized light. *Crit. Rev. Solid State Mater. Sci.* **20**, 179–283 (1995).
166. Wang, Y. H. et al. Observation of a warped helical spin texture in  $Bi_2Se_3$  from circular dichroism angle-resolved photoemission spectroscopy. *Phys. Rev. Lett.* **107**, 207602 (2011).
167. Weinelt, M. Time-resolved two-photon photoemission from metal surfaces. *J. Phys. Condens. Matter* **14**, R1099–R1141 (2002).

168. Petek, H. & Ogawa, S. Femtosecond time-resolved two-photon photoemission studies of electron dynamics in metals. *Prog. Surf. Sci.* **56**, 239–310 (1997).
169. Ge, N.-H., Wong, C. M. & Harris, C. B. Femtosecond studies of electron dynamics at interfaces. *Acc. Chem. Res.* **33**, 111–118 (2000).
170. Hellmann, S. et al. Time-domain classification of charge-density-wave insulators. *Nat. Commun.* **3**, 1069 (2012).
171. Haight, R. Electron dynamics at surfaces. *Surf. Sci. Rep.* **21**, 275–325 (1995).
172. Hertel, T., Knoesel, E., Wolf, M. & Ertl, G. Ultrafast electron dynamics at Cu(111): response of an electron gas to optical excitation. *Phys. Rev. Lett.* **76**, 535–538 (1996).
173. Hofer, U. Time-resolved coherent photoelectron spectroscopy of quantized electronic states on metal surfaces. *Science* **277**, 1480–1482 (1997).
174. Kirchmann, P. S., Loukakos, P. A., Bovensiepen, U. & Wolf, M. Ultrafast electron dynamics studied with time-resolved two-photon photoemission: intra- and interband scattering in  $C_{60}/Cu(111)$ . *New J. Phys.* **7**, 113–113 (2005).
175. Sobota, J. A. et al. Direct optical coupling to an unoccupied Dirac surface state in the topological insulator  $Bi_2Se_3$ . *Phys. Rev. Lett.* **111**, 136802 (2013).
176. Carpena, E. et al. A versatile apparatus for time-resolved photoemission spectroscopy via femtosecond pump-probe experiments. *Rev. Sci. Instrum.* **80**, 55101 (2009).
177. Rossmagel, K. Shooting electronic structure movies with time-resolved photoemission. *Synchrotron Radiat. News* **25**, 12–18 (2012).
178. Smallwood, C. L., Jozwiak, C. & Lanzara, A. An ultrafast angle-resolved photoemission apparatus for measuring complex materials. *Rev. Sci. Instrum.* **83**, 123904 (2012).
179. Jiang, R. et al. Tunable vacuum ultraviolet laser based spectrometer for angle resolved photoemission spectroscopy. *Rev. Sci. Instrum.* **85**, 33902 (2014).
180. Ishida, Y. et al. Time-resolved photoemission apparatus achieving sub-20-meV energy resolution and high stability. *Rev. Sci. Instrum.* **85**, 123904 (2014).
181. Galitskii, V. M., Goreslavskii, S. P. & Eiesin, V. F. Electric and magnetic properties of a semiconductor in the field of a strong electromagnetic wave. *Sov. Phys. JETP* **30**, 117–122 (1970).
182. Mahmood, F. et al. Selective scattering between Floquet–Bloch and Volkov states in a topological insulator. *Nat. Phys.* **12**, 306–310 (2016).
183. Fregoso, B. M., Wang, Y. H., Gedik, N. & Galitski, V. Driven electronic states at the surface of a topological insulator. *Phys. Rev. B* **88**, 155129 (2013).
184. Koralek, J. D. et al. Laser based angle-resolved photoemission, the sudden approximation, and quasiparticle-like spectral peaks in  $Bi_2Sr_2CaCu_2O_{8+\delta}$ . *Phys. Rev. Lett.* **96**, 17005 (2006).
185. Perfetti, L. et al. Ultrafast electron relaxation in superconducting  $Bi_2Sr_2CaCu_2O_{8+\delta}$ . *Phys. Rev. Lett.* **99**, 197001 (2007).
186. Cortés, R. et al. Momentum-resolved ultrafast electron dynamics in superconducting  $Bi_2Sr_2CaCu_2O_{8+\delta}$ . *Phys. Rev. Lett.* **107**, 97002 (2011).
187. Graf, J. et al. Nodal quasiparticle meltdown in ultrahigh-resolution pump–probe angle-resolved photoemission. *Nat. Phys.* **7**, 805–809 (2011).
188. Rameau, J. D. et al. Photoinduced changes in the cuprate electronic structure revealed by femtosecond time- and angle-resolved photoemission. *Phys. Rev. B* **89**, 115115 (2014).
189. Zhang, W. et al. Ultrafast quenching of electron–boson interaction and superconducting gap in a cuprate superconductor. *Nat. Commun.* **5**, 4959 (2014).
190. Yang, S.-L. et al. Inequivalence of single-particle and population lifetimes in a cuprate superconductor. *Phys. Rev. Lett.* **114**, 247001 (2015).
191. Rameau, J. D. et al. Energy dissipation from a correlated system driven out of equilibrium. *Nat. Commun.* **7**, 13761 (2016).
192. Boschini, F. et al. Collapse of superconductivity in cuprates via ultrafast quenching of phase coherence. *Nat. Mater.* **17**, 416–420 (2018).
193. Rettig, L. et al. Electron–phonon coupling in 122 Fe pnictides analyzed by femtosecond time-resolved photoemission. *New J. Phys.* **15**, 83023 (2013).
194. Yang, L. X. et al. Ultrafast modulation of the chemical potential in  $BaFe_2As_2$  by coherent phonons. *Phys. Rev. Lett.* **112**, 207001 (2014).
195. Avigo, I. et al. Electronic structure and ultrafast dynamics of FeAs-based superconductors by angle- and time-resolved photoemission spectroscopy. *Phys. Status Solidi* **254**, 1600382 (2017).
196. Suzuki, H. et al. Ultrafast melting of spin density wave order in  $BaFe_2As_2$  observed by time- and angle-resolved photoemission spectroscopy with extreme-ultraviolet higher harmonic generation. *Phys. Rev. B* **95**, 165112 (2017).
197. Yang, S. et al. Thickness-dependent coherent phonon frequency in ultrathin  $FeSe/SrTiO_3$  films. *Nano Lett.* **15**, 4150–4154 (2015).
198. Petersen, J. C. et al. Clocking the melting transition of charge and lattice order in  $17-Ta_2S_5$  with ultrafast extreme-ultraviolet angle-resolved photoemission spectroscopy. *Phys. Rev. Lett.* **107**, 177402 (2011).
199. Rettig, L. et al. Persistent order due to transiently enhanced nesting in an electronically excited charge density wave. *Nat. Commun.* **7**, 10459 (2016).
200. Sobota, J. A. et al. Ultrafast optical excitation of a persistent surface-state population in the topological insulator  $Bi_2Se_3$ . *Phys. Rev. Lett.* **108**, 117403 (2012).
201. Hajlaoui, M. et al. Ultrafast surface carrier dynamics in the topological insulator  $Bi_2Te_3$ . *Nano Lett.* **12**, 3532–3536 (2012).
202. Crepaldi, A. et al. Evidence of reduced surface electron–phonon scattering in the conduction band of  $Bi_2Se_3$  by nonequilibrium ARPES. *Phys. Rev. B* **88**, 121404 (2013).
203. Sobota, J. A. et al. Ultrafast electron dynamics in the topological insulator  $Bi_2Se_3$  studied by time-resolved photoemission spectroscopy. *J. Electron Spectrosc. Relat. Phenom.* **195**, 249–257 (2014).
204. Sobota, J. A. et al. Distinguishing bulk and surface electron–phonon coupling in the topological insulator  $Bi_2Se_3$ . *Phys. Rev. Lett.* **113**, 157401 (2014).
205. Hajlaoui, M. et al. Tuning a Schottky barrier in a photoexcited topological insulator with transient Dirac cone electron–hole asymmetry. *Nat. Commun.* **5**, 3003 (2014).
206. Cacho, C. et al. Momentum-resolved spin dynamics of bulk and surface excited states in the topological insulator  $Bi_2Se_3$ . *Phys. Rev. Lett.* **114**, 97401 (2015).
207. Wang, Y. H. et al. Measurement of intrinsic Dirac fermion cooling on the surface of the topological insulator  $Bi_2Se_3$  using time-resolved and angle-resolved photoemission spectroscopy. *Phys. Rev. Lett.* **109**, 127401 (2012).
208. Johannsen, J. C. et al. Direct view of hot carrier dynamics in graphene. *Phys. Rev. Lett.* **111**, 27403 (2013).
209. Gierz, I. et al. Snapshots of non-equilibrium Dirac carrier distributions in graphene. *Nat. Mater.* **12**, 1119–1124 (2013).
210. Ulstrup, S. et al. Ultrafast dynamics of massive Dirac fermions in bilayer graphene. *Phys. Rev. Lett.* **112**, 257401 (2014).
211. Ulstrup, S. et al. Ultrafast electron dynamics in epitaxial graphene investigated with time- and angle-resolved photoemission spectroscopy. *J. Phys. Condens. Matter* **27**, 164206 (2015).
212. Papalazarou, E. et al. Coherent phonon coupling to individual Bloch states in photoexcited bismuth. *Phys. Rev. Lett.* **108**, 256808 (2012).
213. Sterzi, A. et al.  $Sb_{2B_3}$  electron–phonon coupling constant from time- and angle-resolved photoelectron spectroscopy. *Phys. Rev. B* **94**, 81111 (2016).
214. Bostwick, A., Rotenberg, E., Avila, J. & Asensio, M. C. Zooming in on electronic structure: NanoARPES at SOLEIL and ALS. *Synchrotron Radiat. News* **25**, 19–25 (2012).
215. Sutter, P., Hybertsen, M. S., Sadowski, J. T. & Sutter, E. Electronic structure of few-layer epitaxial graphene on Ru(0001). *Nano Lett.* **9**, 2654–2660 (2009).
216. Brown, L. et al. Polycrystalline graphene with single crystalline electronic structure. *Nano Lett.* **14**, 5706–5711 (2014).
217. Johansson, L. I. et al. Multiple  $\pi$ -bands and Bernal stacking of multilayer graphene on C-face SiC, revealed by nano-angle resolved photoemission. *Sci. Rep.* **4**, 4157 (2015).
218. Lin, L. et al. Tuning chemical potential difference across alternately doped graphene P–N junctions for high-efficiency photodetection. *Nano Lett.* **16**, 4094–4101 (2016).
219. Pierucci, D. et al. Band alignment and minigaps in monolayer  $MoS_2$ –graphene van der Waals heterostructures. *Nano Lett.* **16**, 4054–4061 (2016).
220. Yuan, H. et al. Evolution of the valley position in bulk transition-metal chalcogenides and their monolayer limit. *Nano Lett.* **16**, 4738–4745 (2016).
221. Wang, E. H. et al. Electronic structure of transferred graphene/h-BN van der Waals heterostructures with nonzero stacking angles by nano-ARPES. *J. Phys. Condens. Matter* **28**, 444002 (2016).
222. Chen, C., Maria, C., Zhang, C., Song, J. & Chen, C. Electronic structure of graphene/hexagonal boron nitride heterostructure revealed by nanoARPES. *J. Phys. Conf. Ser.* **864**, 012005 (2017).
223. Wilson, N. R. et al. Determination of band offsets, hybridization, and exciton binding in 2D semiconductor heterostructures. *Sci. Adv.* **3**, e1601832 (2017).
224. Arango, Y. C. et al. Quantum transport and nano angle-resolved photoemission spectroscopy on the topological surface states of single  $Sb_2Te_3$  nanowires. *Sci. Rep.* **6**, 29493 (2016).
225. Kar, N., Zheng, B., Sun, Y., Fa-xian, X. & Tong-tong, Z. Nano-angle resolved photoemission spectroscopy on topological insulator  $Sb_2Te_3$  nanowires responsible of quantum transport. *J. Phys. Conf. Ser.* **864**, 12041 (2017).
226. Fu, L. & Kane, C. L. Topological insulators with inversion symmetry. *Phys. Rev. B* **76**, 45302 (2007).
227. Fu, L., Kane, C. L. & Mele, E. J. Topological insulators in three dimensions. *Phys. Rev. Lett.* **98**, 106803 (2007).
228. Emma, P. et al. First lasing and operation of an ångström-wavelength free-electron laser. *Nat. Photonics* **4**, 641–647 (2010).
229. Patterson, B. D. et al. Coherent science at the SwissFEL X-ray laser. *New J. Phys.* **12**, 35012 (2010).
230. Allaria, E. et al. Tunability experiments at the FERMI@ Elettra free-electron laser. *New J. Phys.* **14**, 113009 (2012).
231. Yabashi, M. et al. Compact XFEL and AMO sciences: SACLA and SCSS. *J. Phys. B* **46**, 164001 (2013).
232. Kang, H.-S., Kim, K.-W. & Ko, I. S. Status of PAL-XFEL. *Proc. SPIE Vol.* **9512**, 95120P (2015).
233. Pellegrini, C. X-ray free-electron lasers: from dreams to reality. *Phys. Scr.* **T169**, 14004 (2016).
234. Wurth, W. FLASH: running two FELs in parallel. *Synchrotron Radiat. News* **30**, 3–6 (2017).
235. Altarelli, M. The European X-ray Free-Electron Laser: toward an ultra-bright, high repetition-rate X-ray source. *High Power Laser Sci. Eng.* **3**, e18 (2015).
236. Gottlieb, K., Hussain, Z., Bostwick, A., Lanzara, A. & Jozwiak, C. Rapid high-resolution spin- and angle-resolved photoemission spectroscopy with pulsed laser source and time-of-flight spectrometer. *Rev. Sci. Instrum.* **84**, 93904 (2013).
237. Jozwiak, C. et al. Spin-polarized surface resonances accompanying topological surface state formation. *Nat. Commun.* **7**, 13143 (2016).
238. Cao, Y. et al. Correlated insulator behavior at half-filling in magic-angle graphene superlattices. *Nature* **556**, 80–84 (2018).
239. Cao, Y. et al. Unconventional superconductivity in magic-angle graphene superlattices. *Nature* **556**, 43–50 (2018).

## Acknowledgements

The authors thank N. Gedik, A. Zong, B. Fichera, C. Belvin, N. Koirala and Y. Su for useful discussions and feedback in the preparation of this manuscript. This work was supported by the Ministry of Science and Technology of China (grant nos 2016YFA0401000, 2016YFA0300600 and 2015CB921300), the Chinese Academy of Sciences (grant nos XDB28000000, XDB07000000 and QYZDB-SSW-SLH043), the National Natural Science Foundation of China (grant nos 11622435 and U1832202) and the Beijing Municipal Science and Technology Commission (grant no. Z171100002017018). B.Q.L. acknowledges support from the National Science Foundation under grant no. NSF DMR-1809815 (data analysis) and the Gordon and Betty Moore Foundation's EPIQS Initiative grant GBMF4540 (manuscript writing).

## Author contributions

All authors contributed to the discussion of content and researched data for the article. B.Q.L. wrote the manuscript with critical input from H.D. and T.O.

## Competing interests

The authors declare no competing interests.

## Publisher's note

Springer Nature remains neutral with regard to jurisdictional claims in published maps and institutional affiliations.

## Supplementary information

Supplementary information is available for this paper at <https://doi.org/10.1038/s42254-019-0088-5>.

## RELATED LINKS

ARTOF-2 analyser: <https://www.scientaomicron.com/en/products/artoff2/instrument-concept>  
 DA30-L spin spectrometer: <https://www.scientaomicron.com/en/products/353/1170>  
 LCLS-II: <https://lcls.slac.stanford.edu/instruments/lzsi>  
 Roentdek delay-line detectors: [http://www.roentdek.de/info/Delay\\_Line/](http://www.roentdek.de/info/Delay_Line/)  
 VUV5k He lamp: <https://www.scientaomicron.com/en/products/359/1231>